TÉCNICO LISBOA

Multi-Echo Gradient-Echo Spin-Echo with Echo-Planar Imaging for simultaneous quantification of T2* and T2

Joana Rita Mayer Rodrigues Vera-Cruz

Thesis to obtain the Master of Science Degree in

Biomedical Engineering

Supervisors: Prof. Sebastian Weingärtner
Prof. Rita Homem de Gouveia Costanzo Nunes

Examination Committee

Chairperson: Prof. João Miguel Raposo Sanches
Supervisor: Prof. Sebastian Weingärtner
Member of the Committee: Prof. Patrícia Margarida Piedade Figueiredo

July 2022

Declaration

I declare that this document is an original work of my own authorship and that it fulfills all the requirements of the Code of Conduct and Good Practices of the Universidade de Lisboa.

Preface

The work presented in this thesis was performed at MARS Lab (Magnetics Resonance Systems Lab) of Delft University of Technology (Delft, The Netherlands), during the period march-august 2021, under the supervision of Prof. Sebastian Weingärtner and Dr. João Tourais, and within the frame of the Erasmus+. The thesis was co-supervised at Instituto Superior Técnico by Prof. Rita Nunes.

Acknowledgments

I would like to thank everyone who helped and supported me throughout the process of researching and writing my master's thesis. Fortunately, I was lucky to have Prof. Rita, Prof. Sebastian and Dr. João as my thesis advisors, all of them were excellent qualified and experienced. I appreciate their time, their care and their knowledge. Most of all, I appreciate how patient they were and how available to support me whenever I needed.

As to the research phase of my thesis, I was honored to be welcomed as a member of MARS Lab for one semester. I am very grateful to Prof. Sebastian and Dr. João for the opportunity and for all the resourcefulness.

It goes without saying that none of this would have been possible without the support from my family and friends.

To my parents and my sisters, I'm thankful for encouraging me to become my best version and always being there when I need.

To Gal, I am very grateful for the endless care and support, at all times.

To William, Gândara And Telma, I am thankful for the debates, the sharing of knowledge and the friendship.

Last but certainly not least, I wish to express my gratitude to my extended family, Helena, Gilberto and Arcelina. They played a special role in this process, by supporting me and making my life easier with acts of kindness.

To all mentioned above, thank you very much.

Abstract

Motivation: T_2* and T_2 contrast-based sequences provide complementary information for MR applications. The Gradient-Echo and Spin-Echo (GESE) sequence has been developed to facilitate the simultaneous acquisition of T_2* and T_2-weighted images.

Objective: Corroborate the results reported in existing studies that tested the GESE sequence with EPI readout in the myocardium, WM and GM.

Methods: The GESE sequence was implemented through pulse programming by modifying the standard implementation of the ME-GE with EPI readout. Two variations tested - with simple and with composite refocusing pulses. Phantom scans and in-vivo scans of two healthy volunteers were conducted. Subsequently, a pixel-wise least squares fit was performed for computing quantitative T_2* and T_2 maps, from which ROIs were defined and mean values were extracted.

Results: Results obtained with simple and composite refocusing pulses, were respectively: for WM T_2*: (55 ± 1 ; 52 ± 2) ms , T_2: (64 ± 2 ; 64 ± 4) ms , for GM (T_2*: 57 ± 2 ; 56 ± 3) ms , T_2: (78 ± 5; 80 ± 8) ms and for Myocardium T_2*: (25 ± 10 , 27 ± 12) ms; T_2: (34 ± 14, 46 ± 32) ms.

Conclusions: The values of T_2* and T_2 using the GESE sequence with composite pulse, for the myocardium and WM were similar to the ones reported in literature and generated relative errors between 1.6 and 6.1%. For GM, both values were more distant from to the ones reported in literature, with relative errors of 12.0% and 12.7%.

Keywords: Gradient-Echo Spin-Echo, EPI readout, T_2* mapping, T_2 mapping, Quantitative MRI;

Resumo

Motivação: As sequências com contraste T_2* e T_2 fornecem informações complementares em aplicações de RM. Assim, a sequência GESE foi desenvolvida para facilitar a aquisição simultânea de imagens com contraste T_2* e T_2.

Objetivos: Corroborar os resultados relatados nos estudos existentes que testaram a sequência GESE com EPI no miocárdio, substância branca (SB) e substância cinzenta (SC).

Métodos: A sequência GESE foi implementada através de programação de sequências de pulsos. Duas variações foram testadas - pulso de refasamento simples e pulso de refasamento composto. Foram conduzidos testes em fantomas e em dois voluntários saudáveis. Seguidamente, foi feito um ajuste dos mínimos quadrados por pixel para calcular mapas quantitativos de T_2* e T_2, do quais ROIs foram definidos e respetivos valores médios foram extraídos.

Resultados: Os resultados obtidos com pulsos simples e composto foram, respetivamente: para SB T_2*: (55 $\pm$ 1 ; 52 $\pm$ 2) ms , T_2: (64 $\pm$ 2 ; 64 $\pm$ 4) ms , for SC (T_2*: 57 $\pm$ 2 ; 56 $\pm$ 3) ms , T_2: (78 $\pm$ 5; 80 $\pm$ 8) ms e para o miocárdio T_2*: (25 $\pm$ 10 , 27 $\pm$ 12) ms; T_2: (34 $\pm$ 14, 46 $\pm$ 32) ms.

Conclusões: Os valores de T_2* e T_2 usando a sequência GESE com pulso composto no miocárdio, SB e SC foram semelhantes aos relatados na literatura (erros relativos entre 1,6 e 6,1%). Para a SC, os valores obtidos foram mais distantes em comparação com a literatura (erros relativos de 12,0% e 12,7%).

Palavras Chave: Gradiente-Eco Spin-Eco, Imagem Echo-Planar, Mapeamento de T_2*, Mapeamento de T_2, RM Quantitativa

Contents

List of Figures

List of Tables

Listings

Acronyms

RF	Radiofrequency
NMR	Nuclear Magnetic Resonance
MRI	Magnetic Resonance Imaging
MR	Magnetic Resonance
FA	Flip Angle
CSF	Cerebral Spinal Fluid
BOLD	Blood Oxygenation Level-Dependent
FID	Free Induction Decay
FT	Fourier Transform
SNR	Signal to Noise Ratio
CNR	Contrast to Noise Ratio
EPI	Echo Planar Imaging
ETL	Echo Train Length
GE	Gradient-Echo
MEGE	Multi-Echo Gradient-Echo
FFE	Fast-Field Echo
TE	Echo Time
SE	Spin-Echo
MESE	Multi-Echo Spin-Echo

ETL	Echo Train Length
GESE	Gradient-Echo and Spin-Echo
PPE	Pulse Programming Environment
GOAL-C++	Gyroscan Object-Oriented Acquisition Language
qMRI	Quantitative Magnetic Resonance Imaging
ISMRM	International Society for Magnetic Resonance in Medicine
NIST	National Institute of Standards and Technology
FOV	Field Of View
TR	Repetition Time
SENSE	SENSitivity Encoding
GVE	Graphical Viewer Environment
ROI	Region Of Interest
SD	Standard Deviation
DICOM	Digital Imaging and Communications in Medicine
SPIR	Spectral Presaturation with Inversion Recovery
SPAIR	Spectrally Selective Attenuated Inversion Recovery
TSE	Turbo Spin-Echo
TFE	Turbo Field Echo
SW	Susceptibility-Weighted
fMRI	Functional Magnetic Resonance Imaging
CMR	Cardiovascular Magnetic Resonance Imaging
PI	Parallel Imaging
PWI	Perfusion Weighted Imaging
WM	White matter
GM	Gray matter

1

Introduction

1.1 Nuclear Magnetic Resonance

The phenomenon of Nuclear Magnetic Resonance (NMR), as the name suggests, is the underlying principle of Magnetic Resonance Imaging (MRI) and it was demonstrated in water for the first time by Felix Bloch in 1945 [17]. NMR describes the interaction of nuclear spins with two main magnetic fields, a static field B_0, and an oscillating Radiofrequency (RF) field B_1. The atoms that present NMR have an odd number of protons and/or neutrons and therefore have nuclear spin angular momentum. For simplicity, these nuclei can be referred to as spins [1]. The hydrogen atom (^{1}H), with one proton, for being the most abundant in the human body, is commonly targeted in MRI and provides a good example to look at.

The proton of ^{1}H can be seen as a spinning charge, which gives rise to a magnetic moment pointing up if the proton is spinning in a clock-wise direction and vice versa. This way, the ^{1}H acts as a small "magnet" and in the presence of an external magnetic field B_0 its magnetic moment vector aligns with the direction of B_0 - by convention, the z-direction. However, this alignment is not perfect, since the spin also precesses around B_0 at a defined frequency, known as the Larmor frequency, defined by the

following equation:

$$\omega_0 = \gamma B_0, \tag{1.1}$$

where γ is the gyromagnetic ratio of the atom. For ^{1}H, γ = 48.52 MHz/Tesla.

This precession phenomenon is also known as resonance. The sum of the magnetic moment of all spins affected by B_0 averaged together results in a net magnetic moment vector M along the z-direction with strength M_0.

If B_0 = 3T, the Larmor frequency of the spin system is given by $48.52 \cdot 3 = 145.56$ MHz, within the RF region. Hence, it is possible to excite the spins by applying a RF magnetic pulse B_1 along the XY plane that rotates at the Larmor frequency.

This will cause the net magnetization vector to "tip" to the XY plane while precessing about the z-axis, with a Flip Angle (FA) dependent on the duration and strength of B_1. Figure 1.1 illustrates the behavior of the magnetization vector during excitation with FA of 90°.

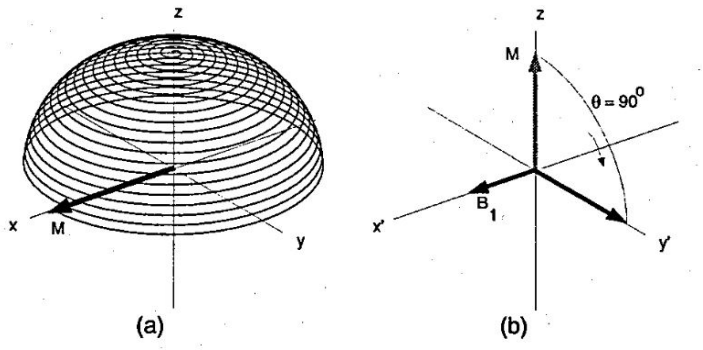

Figure 1.1: The behavior of the magnetization vector M upon excitation by the RF field B_1 with FA = 90°, represented in different frames of reference; a) Nutation of M in the laboratory frame of reference; b) Tipping of M in the rotating frame of reference. Adapted from [1].

When excitation is turned off, spins initiate a process known as relaxation, which comprises a series of energetic exchanges and interactions between spins and their surroundings, leading the magnetization vector to return to equilibrium.

Relaxation processes can be divided into two independent types: longitudinal and transverse relaxation. The first refers to the return of the magnetization vector along the z-axis (longitudinal axis) while the second refers to the decay of the magnetization vector in the XY plane (transverse plane).

Longitudinal relaxation is also known as T_1 relaxation or spin-lattice relaxation or thermal relaxation because it involves exchanges of thermal energy between the spins and nearby atoms and molecules through electromagnetic interactions, collisions and rotations [5]. Similarly to excitation, the energy exchange is induced by fluctuating magnetic fields at the Larmor frequency with an XY component. These field fluctuations are caused by the motion of near magnetic dipoles and promote transitions from

spin-down orientation (higher energy) to spin-up orientation (lower energy). As a result, M_z grows back to M_0 and the spin system achieves thermal equilibrium.

The evolution of M_z can be modeled according to [1]:

$$M_z(t) = M_0 + (M_z(0) - M_0)e^{\frac{-t}{T_1}} \tag{1.2}$$

And for the case of a 90° excitation, $M_z(0) = 0$, thus:

$$M_z(t) = M_0(1 - e^{\frac{-t}{T_1}}), \tag{1.3}$$

where T_1 is a first-order time constant known as the spin-lattice time constant.

It is important to note that according to Equation 1.1 if B_0 increases, ω increases proportionally. For this relaxation, higher values of ω require energy transfer at higher frequencies, which take longer for protons in molecules with intermediate or low mobility. Hence, longitudinal relaxation depends on field strength and increasing values of B_0 result in longer T_1 values.

Transverse relaxation, whose understanding is essential for the work developed in this thesis, will be explained in more detail in the next section.

1.2 Transverse Relaxation and BOLD effect

Transverse relaxation, also referred as spin-spin relaxation or T_2 relaxation, is defined by a group of relaxation processes that occur when B_1 stops being applied, by which the magnetization vector M loses its transverse component. As explained before, after excitation there is a phase coherence of a small fraction of spins that results in a nonzero net transverse magnetization (M_{xy}) and thus any process that results in loss of phase coherence (or dephasing) between spins contributes to this relaxation [5,18].

An important cause of T_2 relaxation is the spin-spin interaction that happens when spins experience different local field disturbances (ΔB_{loc}) besides the main magnetic field (B_0), mainly due to differences in their molecular environment. Consequently, with time, spins will have different local precessional frequencies and accumulate a phase difference between each other.

Taking into account that ΔB_{loc} is in the same direction as B_0, then the phase difference experienced by a spin during T_2 relaxation is given by:

$$\Delta\phi = \gamma \Delta B_{loc} t \tag{1.4}$$

As a result of spin dephasing, the net transverse magnetization (M_{xy}) decreases and reaches zero when all spins are randomly distributed. This effect is represented in Figure 1.2.

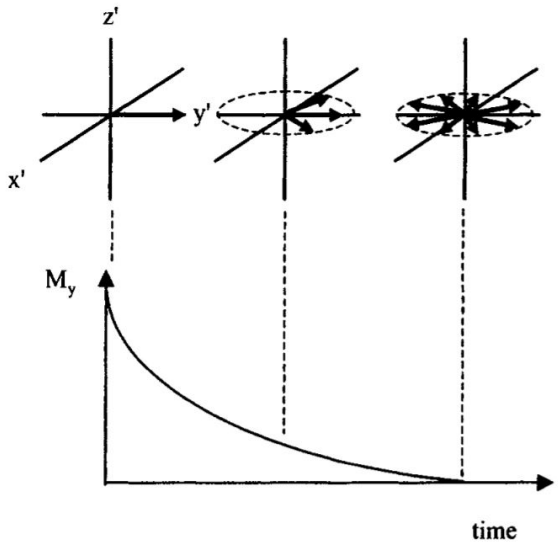

Figure 1.2: The upper diagrams show the magnetic moments of a representative number of spins in the rotating frame. After a 90° excitation, the magnetic moment vectors are tipped to the transverse plane (left diagram) but immediately begin to "fan out", or dephase (middle and right diagrams), as a consequence of transverse relaxation. The graph on the bottom shows the M_y component of the magnetization with time as spin dephasing occurs. (For simplification, longitudinal relaxation is ignored). Adapted from [2].

The decay of M_{xy} is exponential with time constant T_2, also referred to as spin-spin relaxation time [1]. It can be described as follows:

$$\frac{dM_{xy}}{dt} = \frac{-M_{xy}}{T_2} \tag{1.5}$$

The solution to this equation for an arbitrary tip angle α is as follows:

$$M_{xy}(t) = M_0 sin(\alpha) e^{\frac{-t}{T_2}} \tag{1.6}$$

Assuming α = 90°, T_2 can be seen as the time it takes until M = $\frac{1}{e}$ M_0, that is, until it decays to approximately 37% of its initial value. Following this reasoning, the transverse relaxation rate (R_2) is defined by $1/T_2$ and smaller values of T_2 correspond to higher transverse relaxation rates.

T_2 values are tissue-specific and vary mainly with molecular rotation. The relevant field fluctuations that contribute to T_2 relaxation are those near zero frequency [1], because they exert a permanent bias on the local magnetic field and change the Larmor frequency of the spins. This is the case of solids, macromolecules and bound water molecules, where motion is constrained and T_2 is in the order of microseconds. In contrast, T_2 values increase (slower relaxation) if molecular rotation is faster because the influence of neighboring molecules on the local magnetic field changes rapidly and the overall effects tend to cancel out [19, 20]. Some examples of tissues with higher values of T_2 are free water and Cerebral Spinal Fluid (CSF), where the T_2 values are in the order of seconds. T_2 is relatively in-

dependent of the field strength in the clinical MR imaging range (0.2-3T) considering that the slow field fluctuations that cause this relaxation are not affected by a shift in Larmor frequency [5]. Table 1.1 shows experimental T_2 values extracted from the literature for the myocardium, White matter (WM) and Gray matter (GM) at 3T.

Table 1.1: Values of T_2 for ^1H protons in human brain and heart at B_0 = 3T.

Tissue	T_2 (ms) mean ± SD	Reference
Myocardium	67 ± 5	[21]
Gray Matter	83 ± 4	[21]
White Matter	75 ± 3	[21]

The events described above that contribute to T_2 decay do not fully describe the transverse relaxation rate. In reality, the observed rate at which M_{xy} decays is much faster due to additional external field inhomogeneities [5]. These are caused by two main sources. The first are intrinsic defects in magnet design, as it is impossible to produce a magnet that generates a perfectly uniform magnetic field. The second is susceptibility-induced field distortions that can arise from air/tissue, bone/tissue boundaries, local deposits of iron, or other materials placed within the field. These factors are described in the literature by a separate time constant known as T_2'. Therefore, the total relaxation rate (R_2*) is given by [22]:

$$R_2^* = R_2 + R_2' \tag{1.7}$$

This can be rewritten as a function of the relaxation times, as follows:

$$\frac{1}{T_2^*} = \frac{1}{T_2} + \frac{1}{T_2'} \tag{1.8}$$

An illustrative representation of signal decay with relaxation rates R_2 and R_2* is provided in Figure 1.3. Table 1.2 presents experimental T_2* values extracted from the literature for myocardium, WM and GM at 3T.

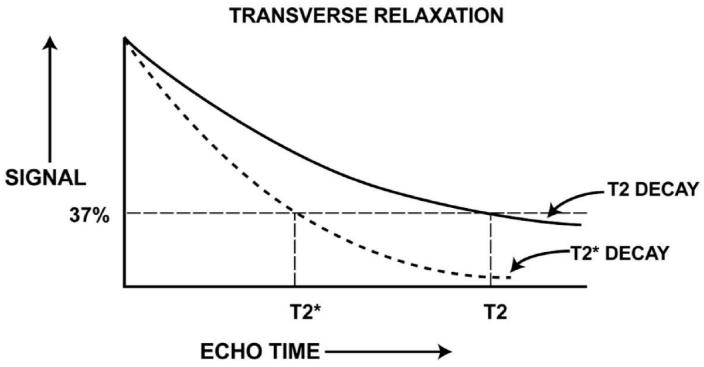

Figure 1.3: Signal decay with T_2 and T_2*. Retrieved from [3].

Table 1.2: Values of T_2* for ^{1}H protons in human brain and heart at B_0 = 3T.

Tissue	T_2* (ms) mean ± SD	Reference
Myocardium	24 ± 5	[23]
Gray Matter	59.9 ± 3.0	[24]
White Matter	43.5 ± 1.8	[24]

T_2 and T_2* quantification provides relevant information regarding tissue structure and function. An example of the latter is blood oxygenation. This is because hemoglobin changes its magnetic properties whether it is bonded or not to oxygen, referred to as oxyhemoglobin and deoxyhemoglobin, respectively. Deoxyhemoglobin is strongly paramagnetic due to its four unpaired electrons at each iron center and therefore contributes to transverse dephasing and shortens both T_2 and T_2* [5]. This phenomenon is known as the Blood Oxygenation Level-Dependent (BOLD) effect.

1.3 Magnetic Resonance Imaging

This section aims to introduce the imaging gradients that are involved in the spatial encoding of the Magnetic Resonance (MR) signal and to explain how an image is obtained from the signal measured.

1.3.1 Slice Selection Gradients

Slice selection gradients are needed to spatially target spins of interest and they are used concurrently with selective RF pulses [4,5,20]. They consist of applying a linearly variable magnetic field in a direction perpendicular to the desired slice plane. This way, each slice experiences a different magnetic field, and

therefore, frequency (see Equation 1.1), according to its position along the gradient axis, that can be expressed as:

$$F_{\mathrm{c}} = \gamma(B_0 + zGss), \tag{1.9}$$

where F_{c} corresponds to the slice center frequency, z corresponds to the position of the slice, along the z-axis (in the case where the gradient is applied along z), and Gss is the strength of the slice selection gradient.

It is important to note that the slices have a specific thickness (Δz) value and therefore, in the presence of a slice selection gradient, they experience a range of frequencies (Δf) around their center frequency. Δf corresponds to the transmitter RF bandwidth, i.e., the range of frequencies in the RF pulse. This can be easily derived from Equation 1.9, resulting in:

$$\Delta f = \gamma Gss \Delta z \tag{1.10}$$

Equation 1.10 shows that, for a fixed Δf, stronger gradients produce thinner slices and vice versa. These concepts are summarized in Figure 1.4.

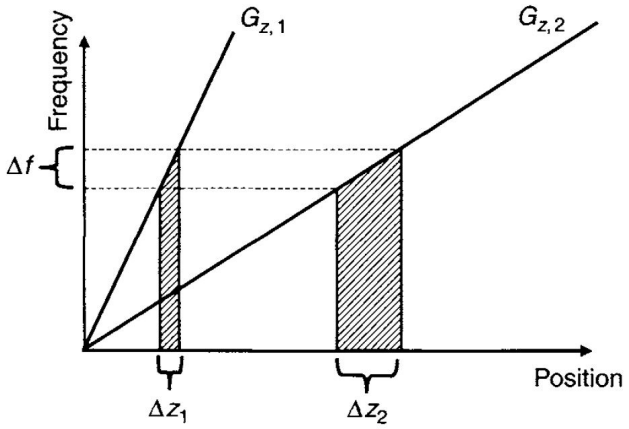

Figure 1.4: Slice thickness is proportional to the transmitter RF bandwidth and inversely proportional to the slice selection gradient strength. Steep gradients and narrow Δf's produce thin slices and vice versa. Retrieved from [4].

When a slice selection gradient is applied with an excitation RF pulse, its effect is similar to a spoiler gradient from the isodelay of the pulse, meaning that it forces phase dispersion and, therefore, signal loss. To compensate for this phase dispersion of the transverse magnetization, it is common to use a slice rephasing lobe, also known as slice refocusing lobe, with opposite polarity to the previous slice selection gradient.

However, with refocusing RF pulses, the second half of the slice selection gradient compensates for

the phase accumulated during the first half of the gradient. Therefore, rephasing lobes are not employed.

There are other gradients, applied along the slice selection direction, that are important to mention, such as crusher gradients. Crusher gradients are often implemented in pairs, G_L and G_R, before and after an RF pulse, with equal area and polarity. The right crusher is used to eliminate unwanted Free Induction Decay (FID) signals that arise from pulse design imperfections [5].

Because refocusing pulses have imperfect slice profiles, they also act on spins that don't belong to the selected slice with a flip angle that can be higher or lower than 180°. This generates unpredicted FID signals that interfere with the signal pathway. To avoid that, a crusher gradient, which in this context acts like a spoiler gradient, is placed after the pulse.

However, the right crusher also acts upon the spins of the selected slice, which would lead to spin dephasing and signal loss if no other gradient was applied. For this reason, G_L is placed before the pulse. In the presence of a 180° refocusing pulse, the effect of G_L is canceled by G_R on the spins of interest.

The slice selection, slice rephasing, and crusher gradients are represented in Figure 1.5.

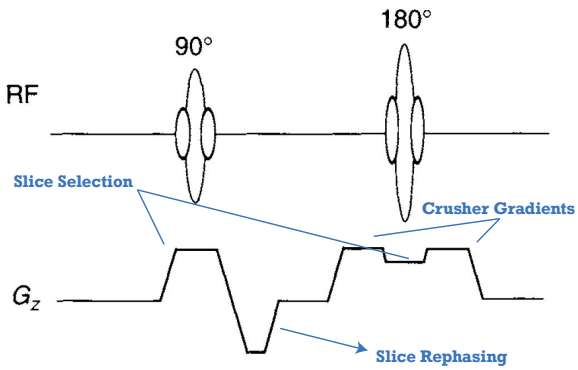

Figure 1.5: Schematics of the slice selection, slice rephasing, and crusher gradients involved in selecting specific slices for imaging. Adapted from [4].

1.3.2 Frequency-Encoding Gradients, Phase-Encoding Gradients, and k-Space

The working principle of all gradients is the same, i.e., they consist of applying a secondary linearly variable magnetic field to make spin resonant frequencies vary as a function of spatial position [5]. Frequency-encoding gradients are implemented along the frequency direction and, combined with phase-encoding gradients, can specify a location within a slice.

Phase-encoding gradients, although working in the same way as frequency-encoding gradients, focus on proton phase shifts as a consequence of resonant frequency variations. This happens because when a gradient is applied for a certain amount of time, it not only induces frequency changes but also

phase shifts, which can be represented as:

$$\Delta\phi = \gamma G \Delta t \tag{1.11}$$

When the gradient is turned off, spins have ”memory” of the gradient effect on them, and, despite returning to resonate at the Larmor frequency, their phase shift remains. Taking into account Equation 1.11, the magnitude of the accumulated phase shift experienced by protons depends on the strength and duration of the gradient. In other words, the accumulated phase shift directly depends on the gradient area.

Figure 1.6(a) shows an illustrative example of frequency and phase encoding of a 2D slice that helps to understand that one phase-encoding step is not enough to find the signal contributions of each pixel.

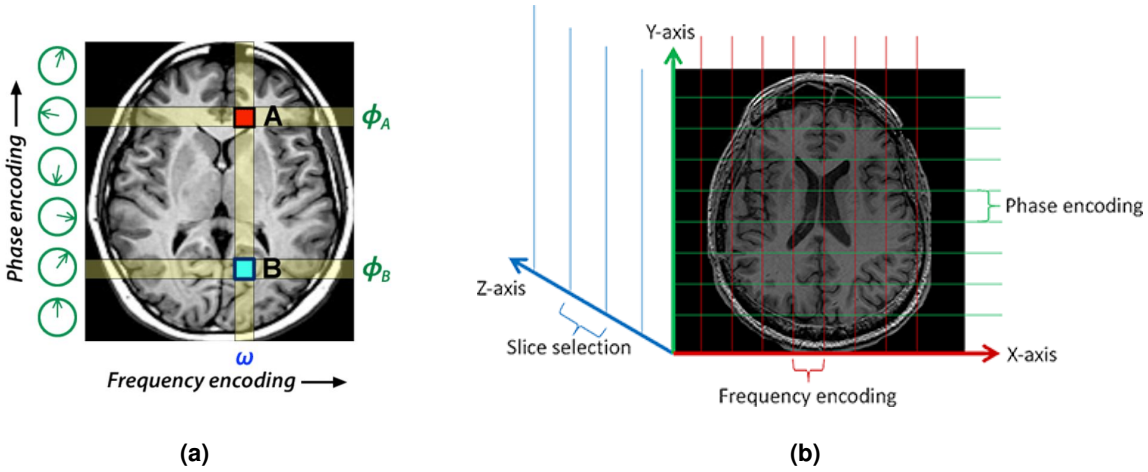

(a) **(b)**

Figure 1.6: **(a)** The frequency-encoding gradients are applied along the frequency direction and make spin resonant frequencies vary as a function of spatial position. The phase-encoding gradients cause different phase shifts to spins along the phase direction, which is perpendicular to the frequency direction, which depends on the gradient area. Retrieved from [5]. **(b)** Slice selection, frequency-encoding gradients, and phase-encoding gradients induce the same effects on protons but are applied in different directions for different purposes. Slice selection gradients allow spatial specification between slices and frequency-encoding gradients combined with phase-encoding gradients, allow for spatial specification within a slice. Retrieved from [6]

Considering only pixels A and B, for simplicity reasons, which belong to the same column, we can assume that after a frequency-encoding gradient is applied along the longitudinal axis, they possess the same resonant frequency ω. Pixel A has signal $A \cdot sin(\omega t)$ and pixel B has signal $B \cdot sin(\omega t)$ but the measured signal consists of the sum of the signal from each pixel, which in this case is $S_0 = (A + B) \cdot sin(\omega t)$. With one signal measurement, it is not possible to know the individual values of A and B, only their sum.

However, if we perform a second measurement after a phase-encoding step considering that pixel A was in the location of zero gradient strength and that pixel B was in the location of maximum gradient

strength, the signal of pixels A and B is $A \cdot sin(\omega t)$ and $-B \cdot sin(\omega t)$. This time, the signal sum is $S_1 = (A - B) \cdot sin(\omega t)$ and despite A and B being unknown, the value of their difference is known. By combining the equations of S_0 and S_1, it is now possible to compute the values of A and B using basic algebra. Since in a real MR image, there are usually hundreds of pixels to take into account, hundreds of phase-encoding steps are needed to assign all the pixel values.

Figure 1.6(b) shows the conventional slice selection, frequency-encoding, and phase-encoding directions, along the z, x, and y-axis, respectively, for better understanding.

As explained previously, frequency-encoding and phase-encoding gradients are used to encode pixel data, and when the MR signal is measured, these data are stored in a matrix known as the k-space. The k-space stores all the information of an MR image in a matrix of spatial frequencies. These spatial frequencies correspond to the number of wave cycles per unit distance along the x or y-axis and are designated k_x and k_y, respectively.

The center of the k-space stores the data of lower spatial frequencies of the image, which correspond to the basic contrast, general shapes, and contours. Meanwhile, the periphery of the k-space, which corresponds to higher spatial frequencies, holds the information on the details, sharp transitions, and edges of the image. The phase-encoding gradient steps determine which k-space line is filled (lower-order steps correspond to the lines near the center of k-space and vice versa). This can be observed in Figure 1.7.

It is important to note that the data points in the k-space do not correspond directly to the points of the image. To obtain the MR image from the k-space a 2D Fourier Transform (FT) is needed, and it is achieved by performing a 1D FT in one direction and a second 1D FT in the orthogonal direction, on the result of the previous one.

In MRI there are several techniques to fill the k-space and in this work, we will focus on the Echo Planar Imaging (EPI) technique. Its basic principles, applications, advantages, and disadvantages will be discussed in the next sub-chapter.

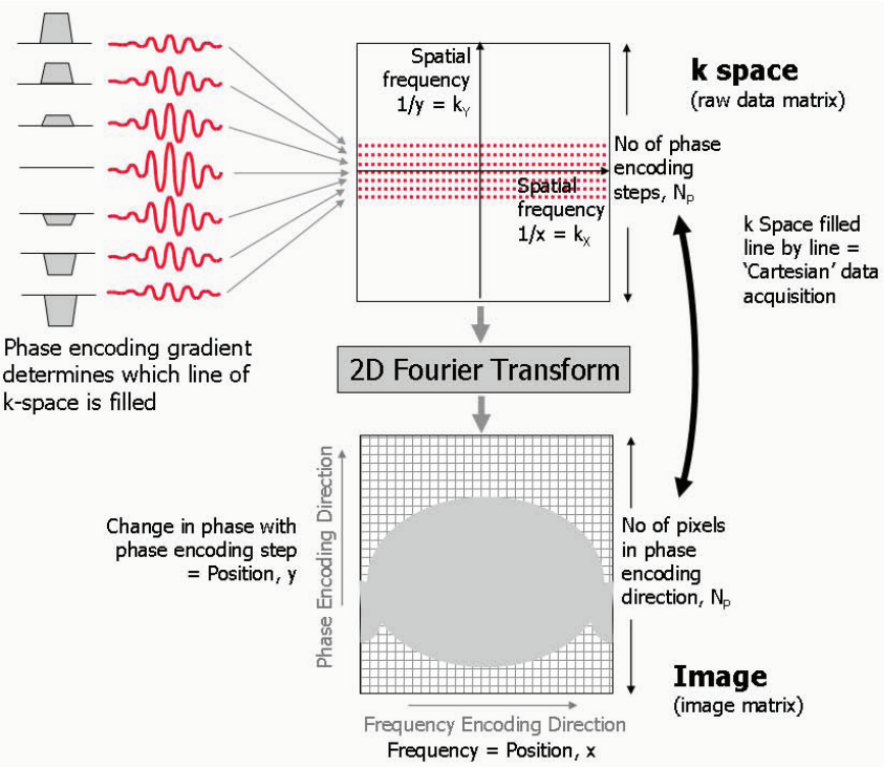

Figure 1.7: k-space stores all the information of the MR image as a matrix of spatial frequencies along the x and y-axis. In the Cartesian data acquisition method, each line of the k-space is filled according to the phase-encoding gradient step applied. To obtain an image from k-space, a 2D inverse FT must be performed. Adapted from [7].

1.3.3 Echo Planar Imaging

Echo Planar Imaging, or EPI, is a fast MRI pulse sequence that collects multiple echoes, or k-space lines, from a single RF pulse with the use of frequency and phase-encoding gradients [4]. The EPI readout (or frequency-encoding) gradients comprise a series of identical lobes with alternating polarity, except the first lobe. The latter is a prephasing gradient, with opposite polarity and half area of the first readout gradient lobe, which is used to bring the k-space trajectory to $k_{x,min}$. The subsequent lobe, with positive polarity, moves the trajectory from $k_{x,min}$ to $k_{x,max}$. From there, the following negative and positive lobes change the trajectory from $k_{x,max}$ to $k_{x,min}$ and from $k_{x,min}$ to $k_{x,max}$, respectively, and so on. Readout gradients do not necessarily need to have the same amplitude or shape, as long as they have the same absolute value of the area, however, they usually do and one of the most common waveforms is the trapezoidal waveform, represented in Figure 1.8(a).

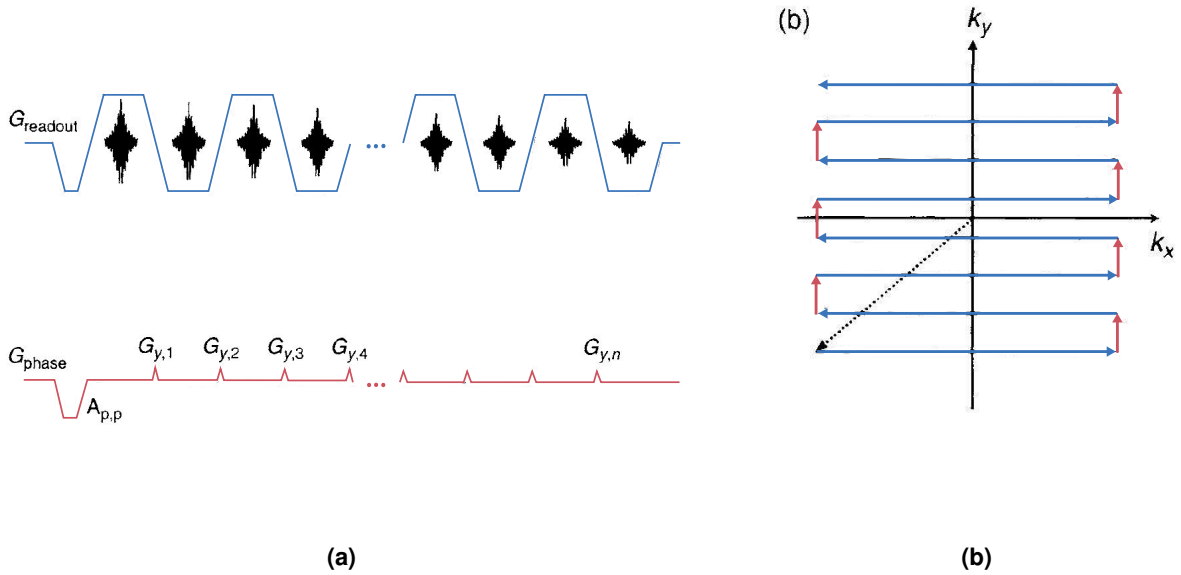

Figure 1.8: (a) Schematics of the EPI readout and phase-encoding gradients. **(b)** EPI k-space trajectory: the dashed arrow points to the initial position of the sampling. The readout gradient lobes move the trajectory along the x-axis and the phase-encoding gradient blips move the trajectory along the y-axis. Adapted from [4].

After each readout gradient lobe, a phase-encoding blip is displayed to move the k-space trajectory along the y-direction. Similar to the readout gradients, the phase-encoding gradients start with a prephasing lobe to place the trajectory at $k_{y,min}$. This way, the initial position of the k-space sampling is $\{ k_{x,min}, k_{y,min} \}$. As a trade-off for its fast k-space sampling, EPI faces many challenges that affect image resolution, Signal to Noise Ratio (SNR) and generate artifacts such as T_2* effects, geometric distortions, ghosting artifacts, and chemical shift artifacts.

Image blurring due to T_2* dephasing effects is also commonly seen in EPI acquisitions, especially if they are long and single-shot. Since each k-space line is acquired at a different time and consequently has a different T_2* weighting, the blurring is seen along the phase encoding direction. Potential solutions for reducing image blurring might include reducing the Echo Train Length (ETL) or the inter echo spacing. Another solution can be changing from a single-shot to a multi-shot acquisition.

1.4 MRI Sequences with T_2* and T_2-based contrast

1.4.1 Gradient-Echo

The Gradient-Echo (GE) sequence is a fast imaging sequence, widely used in vascular and cardiac imaging, that can be used to produce T_2*-based contrast images [4]. The classic single-echo gradient-echo sequence comprises one RF pulse of a chosen FA with a simultaneous slice selection gradient and Cartesian readout (see Figure 1.9).

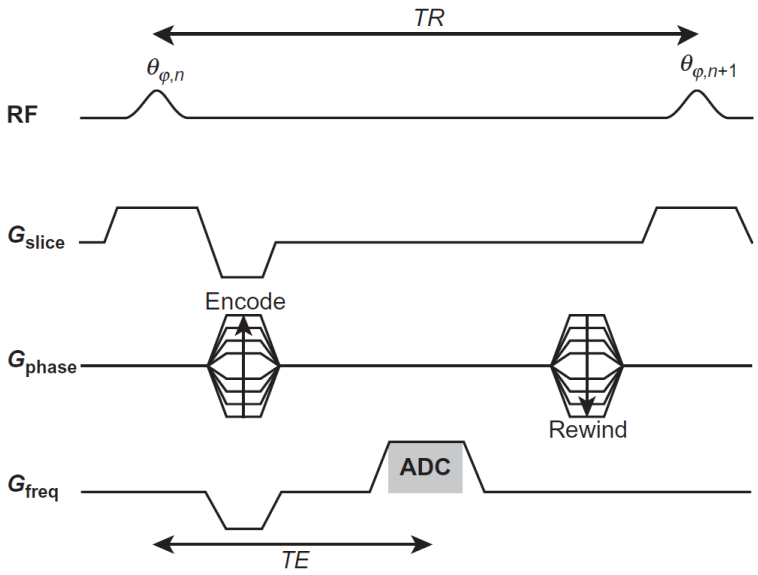

Figure 1.9: Schematics of the RF pulse and gradients involved in a Gradient-echo (GE) sequence (For simplicity, FA = 90°). Adapted from [8].

The echo is formed by combining two frequency gradients with opposite polarity: the prephasing gradient lobe and the readout lobe, which can be combined into a single waveform. The prephasing gradient prepares the spins for a future echo by forcing phase accumulation which, as discussed in section 1.3.2, depends on spin position along the gradient direction. The readout gradient reverses the direction of the phase accumulation and an echo is formed after a time interval after the excitation pulse denoted as Echo Time (TE). The maximum echo signal is achieved when the readout lobe area equals the area of the prephasing lobe (see Figure 1.9).

Even though the readout gradient lobe cancels the gradient-induced dephasing at TE, it does not cancel phase accumulation caused by off-resonance effects such as susceptibility variations and B_0 inhomogeneity. For this reason, the signal measured at TE suffers T_2* decay. While T_2*-weighting can be beneficial for applications such as imaging a hemorrhage, it also leads to signal loss artifacts.

1.4.2 Gradient-Echo with EPI readout

The single-shot EPI readout, as mentioned in 1.3.3, accelerates the acquisition time by allowing the sampling of k-space following a single RF pulse, which helps reduce motion artifacts. Here, the specifics of the GE with EPI readout are discussed.

The GE-EPI sequence usually employs a fat suppression pulse to avoid chemical shift artifacts, a selective excitation pulse, followed by the phase and frequency EPI gradients and a spoiler gradient to dephase the remaining transverse magnetization (see Figure 1.10). Because the Repetition Time (TR) is longer in GE-EPI than in conventional GE with Cartesian readout, the excitation pulse is usually 90° to improve SNR.

As is well known, in EPI each k-space line is acquired at a different echo time, meaning that each line has a different T_2* weighting. The effective TE corresponds to the TE when the center of the k-space is sampled, i.e., TE_{eff}=TE(k_y=0) [4], and it is determined by the area of the prephasing gradient (A_{pp}). Therefore, by adjusting A_{pp} we can control how much T_2* weighting the image will have. At higher B_0 fields, magnetic susceptibilities become more evident and T_2* values are shorter, therefore smaller TE_{eff} values should be used to maintain SNR and image contrast.

Using a faster acquisition readout method such as EPI for T_2*-based contrast imaging improves the monitoring of physiological alterations such as BOLD effects, which is useful for clinical applications such as Functional Magnetic Resonance Imaging (fMRI).

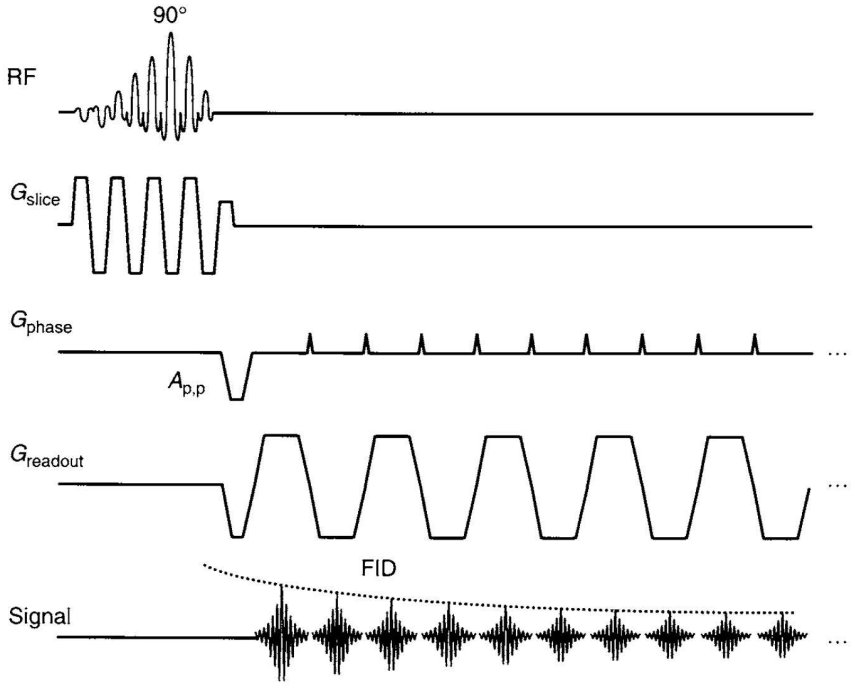

Figure 1.10: Schematics of the GE sequence with EPI readout. Retrieved from [4].

1.4.3 Multi-Echo Gradient-Echo

Multiple gradient echoes can be generated from a single RF pulse by using multiple frequency gradient lobe pairs, with an opposite polarity that continue dephasing and rephasing spins. An example of a Multi-Echo Gradient-Echo (MEGE) sequence with Cartesian readout can be observed in Figure 1.11.

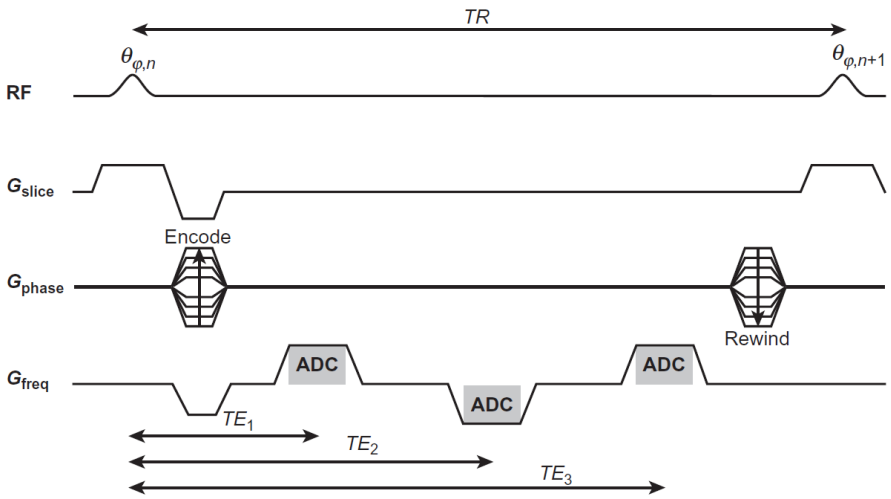

Figure 1.11: Schematics of the RF pulse and gradients involved in a Multi-Echo Gradient-Echo (MEGE) sequence. Adapted from [8].

In general, for imaging tissues with a wide range of T_2* values, the multi-echo gradient-echo sequence is preferred over the single-echo.

1.4.4 Spin-Echo

The Spin-Echo (SE) sequence generates T_2-based contrast images with the use of a refocusing pulse, which is commonly set to 180° after the spin excitation pulse [4]. As explained in Section 1.1, when a 90° excitation pulse is applied, the magnetization vector precesses in the transverse plane, and spins immediately accumulate phase due to T_2 and T_2* decay. To create a spin-echo, a 180° refocusing pulse is played after a time interval TE/2 after the 90° RF pulse, causing to reverse spin direction by 180° in the transverse plane. After the refocusing pulse, spins continue to dephase and at instant TE an echo occurs. This can be observed in Figure 1.12.

To compensate for the dephasing caused by the frequency gradient during readout, a frequency prephasing gradient lobe is placed before the refocusing pulse, with equal polarity. The maximum echo signal occurs when the area under the readout gradient matches the prephasing gradient. It is important to ensure that the slice profiles of the excitation and refocusing pulses match and to use well-designed crusher gradients to avoid incomplete signal refocusing and altered spin-echo slice profile [25].

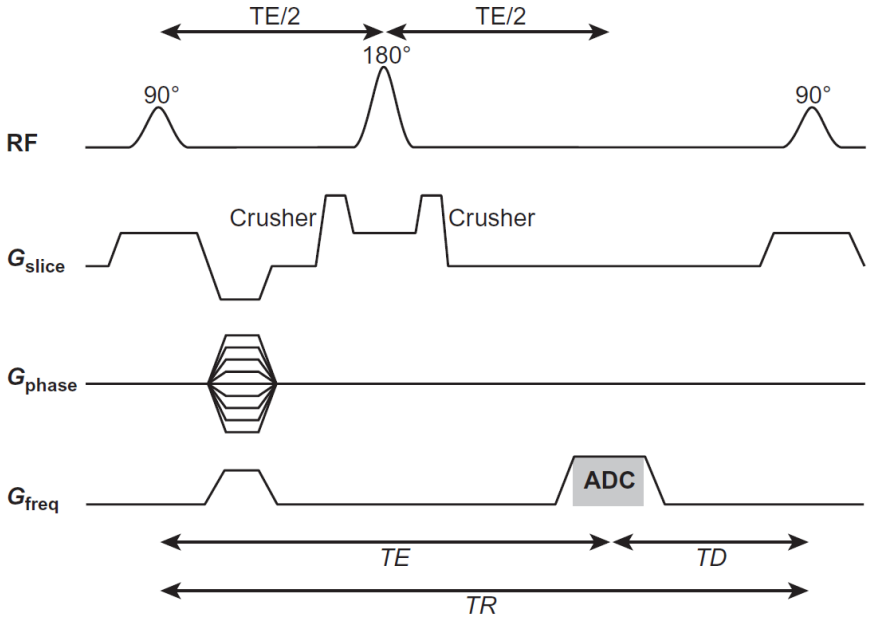

Figure 1.12: Schematics of the RF pulses and gradients involved in a Spin-Echo (SE) sequence with Cartesian readout. Adapted from [8].

Contrarily to the GE sequence, in the SE sequence the off-resonance effects are canceled at TE, meaning that the M_{xy} decays with T_2. SE images are therefore less prone to artifacts due to B_0 inhomogeneity, magnetic susceptibility and chemical shift artifacts. In addition, increasing the TE in SE generates images more heavily T_2-weighted without signal loss due to off-resonance effects.

1.4.5 Multi-Echo Spin-Echo

More spin-echoes can be generated through the use of subsequent RF refocusing pulses in Multi-Echo Spin-Echo (MESE) sequences (see Figure 1.13). The following echoes form an echo train and are designated TE_1, TE_2, TE_3, ... The number of echoes in an echo train is the ETL, which value is limited by the exponential signal decay caused by T_2 decay.

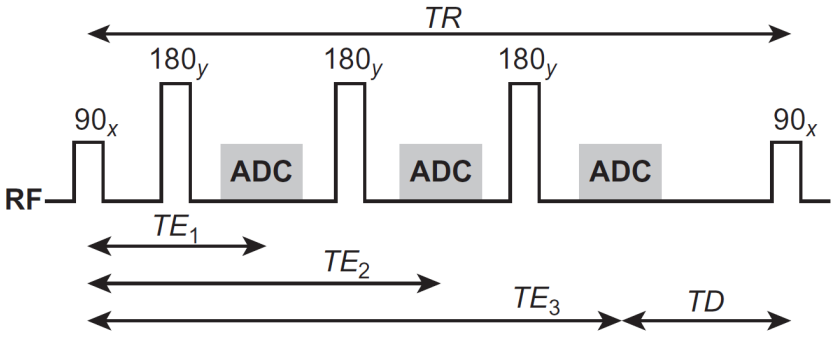

Figure 1.13: Schematic of the RF pulses involved in a Multi-Echo Spin-Echo (MESE) sequence. TD = TR - TE. Adapted from [8].

MESE sequences enable a better sampling of the signal decay after the excitation pulse and can be used to obtain more precise T_2 maps since they provide more data to estimate model parameters.

1.5 State of the Art

Previously, in sections 1.2 and 1.4 the basic principles underlying T_2 and T_2* relaxation were approached, as well as the standard groups of T_2* and T_2-weighted MRI sequences. In this section, the focus is to discuss the factors that affect T_2* and T_2-weighting, the clinical applications of GE and SE sequences, as well as their drawbacks. In addition, the clinical applications and limitations of Gradient-Echo and Spin-Echo (GESE) will be presented, together with the imaging parameters most commonly used for this sequence, as reported in the literature.

GE T_2*-weighted sequences are widely used in several MR applications such has Susceptibility-Weighted (SW) imaging, Perfusion Weighted Imaging (PWI) and fMRI [3].

There are two types of magnetic inhomogeneities that lead to faster T_2* decay: macroscopic inhomogeneities and microscopic inhomogeneities. Macroscopic inhomogeneities are constant within voxels and can be caused by air-tissue boundaries, metallic implants, or deoxyhemoglobin in small veins. Microscopic inhomogeneities change within a voxel and can arise from blood products, iron deposits, or paramagnetic contrast agents.

The amount of T_2* weighting an MR image has can be manipulated through the adjustment of several imaging parameters, more specifically the TE, FA, TR, resolution, and field strength. Increasing TE results in a higher T_2* weighting because if the time interval between excitation and acquisition increases, the spins will have more time to dephase. Low FAs and long TRs contribute to reducing the influence of T_1 decay so that the T_2* differences become dominant. In addition, reducing the resolution, that is, increasing voxel size, will also contribute to more heavily weighted T_2* images because some T_2* dephasing effects occur in large voxels, such as dephasing due to air-tissue boundaries or metal-

lic implants. For the same reason, two-dimensional sequences are more sensitive to T_2* decay than three-dimensional sequences, as they generally use thicker sections. Higher field strengths increase dephasing due to different tissue magnetic susceptibilities and therefore also increase T_2* weighting. Table 1.3 shows an example of acquisition imaging parameters used in different standard implementations of the GE sequence of different vendors.

Table 1.3: Standard GE implementations of different vendors. Note - PRESTO = principles of echo shifting with a train of observations, MPGR = multiplanar GE. Retrieved from [3].

Vendor and Pulse Sequence	Imaging Parameters		
	TR / TE	FA	
Siemens			
Gradient Hemo (RF spoiled GE)	800 / 26	20°	
SWI (SW imaging)	At 3T: 30 / 20	15°	
Philips			
T_2 Fast-Field Echo (FFE)	700 / 23	18°	
EPI T_2*	3500 / 30	90°	EPI Factor, 15
PRESTO (used for perfusion and fMRI)	20 / 8	7°	
GE Healthcare			
MPGR	400 / 15	30°	

Besides its wide range of clinical applications, GE sequences provide more advantages, such as short acquisition times through the use of short TEs and valuable data for Quantitative Magnetic Resonance Imaging (qMRI) and more precise physiological and pathological evaluation of tissues and organs [26]. However, there are some limitations associated with GE sequences, such as low inherent SNR due to the use of low FAs and higher sensitivity to B_0 inhomogeneities.

T_2 contrast-based sequences can help assess the pathological status of the tissues, as it has been proven that the T_2 relaxation times vary between healthy and pathological tissues [27]. An example of an MR application where T_2-based sequences are widely used is Cardiovascular Magnetic Resonance Imaging (CMR). Myocardial tissues with a high water content have higher T_2 relaxation times (slower relaxation times) and therefore appear brighter in the images. As is known for myocardial tissues and other tissues, edema is highly associated with acute injury. T_2-weighted sequences have also been useful for the pathological assessment of other anatomical regions, such as the brain, kidneys, and lungs.

Similarly to T_2*-based sequences, T_2 also employs long TRs to reduce the influence of T_1 decay but long TEs, in the range of the T_2 of the tissue of interest. As expected, the use of longer TEs in T_2*-based sequences can generate signal loss artifacts that can be compensated for by increasing the thickness of the slice at the cost of reduced resolution.

It has been proven that T_2* and T_2 contrast-based sequences provide complementary information on MR applications such as Perfusion Susceptibility Imaging and CMR [28]. In Perfusion Susceptibility Imaging, T_2*-based sequences provide relatively high Contrast to Noise Ratio (CNR) and sensitivity to macro vasculature diameters whereas T_2*-based sequences provide lower sensitivity to contrast agent-induced signal changes but higher sensitivity to microvasculature changes. Therefore, the acquisition on both GE-PWI and SE-PWI is often performed to improve diagnostic value [28]. Additionally, in CMR BOLD MRI techniques can be used to assess myocardial oxygenation with no exogenous contrast agent. In this context, both T_2* and T_2 increase if there are higher concentrations of carbon dioxide in the blood that result in vasodilation. [15]. Hence, GESE sequence has been developed to facilitate the simultaneous acquisition of GE and SE [9, 16, 29–32].

In summary, the GESE sequence, depicted in Figure 1.14, comprises the application of an excitation pulse, followed by two GE acquisitions and after the second acquisition a refocusing pulse is applied, followed by three mixed SE acquisitions. This sequence allows the simultaneous quantification of T_2* and T_2 through the data to the signal equation.

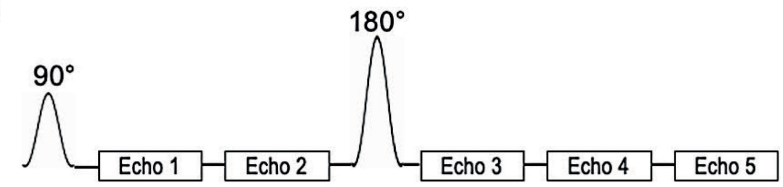

Figure 1.14: Sequence schematics of the GESE. The GESE acquires two GE echoes and three mixed SE echoes. Retrieved from [9].

To capture subtle NMR relaxation effects GESE has been implemented with EPI readout high temporal resolution. In order to reduce readout times and avoid geometric distortions due to T_2* dephasing, Parallel Imaging (PI) techniques, such as SENSitivity Encoding (SENSE), can be combined with EPI [16]. Table 1.4 shows two different examples of previous studies where the GESE sequence was implemented with EPI and SENSE and tested in-vivo in the heart and brain, retrieved from Boomen et al. [15] and Skinner et al. [16]. Furthermore, the values of T_2* and T_2 obtained by Boomen et al. [15] and Skinner et al. [16] are shown in Table 1.5.

The main disadvantages of the GESE sequence include EPI related artifacts, such as relaxation-induced blurring and B_0 distortions. In addition, GESE is acquired with a limited number of slices and spatial resolution so that the temporal resolution penalty enables the detection of subtle BOLD changes.

Table 1.4: Implementations of the GESE sequence with EPI and SENSE, retrieved from Boomen et al. [15] and Skinner et al. [16].

Reference	Purpose	Anatomical Region	Nr of Healthy Participants	Imaging Parameters at 3T								
				Fast Imaging Technique	TE (GE) (ms)	TE (mixed-SE) (ms)	TR (ms)	in-plane Resolution (mm)	Sl. Thick. (mm)	Field Of View (FOV) (mm)	SENSE Factor	Partial Fourier Factor
[15]	Use GESE EPI for quantitative heartbeat-to-heartbeat BOLD response imaging.	Heart (septum)	18	EPI	9.8/23.6	37.8/51.9/66.1	TR = RR, readout/window = 120	2.8×2.8-3.0×3.0	6	350×480	2	37.5% = 0.63
[16]	Evaluating the effect of SENSE PI and PF acceleration on GESE EPI.	Brain	4	EPI	8.3/24	50/66/82	1800	3.16×3.16	5	240×240	2	0.73

Table 1.5: T_2* and T_2 values of the human heart and brain obtained by Boomen et al. [15] and Skinner et al. [16], respectively.

Reference	Results (mean±SD)
[15]	T_2* (ms) = 27.5±4.8 T_2 (ms) = 43.4±5.1
[16]	White matter R_2* (s^{-1}) = 20.21±2.25 [T_2* (ms) = 49.48] R_2 (s^{-1}) = 15.95±1.49 [T_2 (ms) = 62.7] Gray matter R_2* (s^{-1}) = 19.82±6.41 [T_2* (ms) = 50.45] R_2 (s^{-1}) = 14.04±2.42 [T_2 (ms) = 71.22]

1.6 Objectives

Given that very few reports have so far been published regarding the use of the GESE-EPI sequence for BOLD MRI techniques, this work has as its principal objectives the expansion of the available body of literature and the corroboration of the results reported in existing studies that tested this sequence in the human brain and heart. In addition, this study aims to complement the previous development of GESE-EPI by its application in different a MRI scanner.

Moreover, at the beginning of this study an additional objective was set, which consisted of implementing the GESE sequence with spiral readout. However, given the time restriction, this objective was dropped.

2

Methods

2.1 Sequence Validation Protocol

Since the GESE sequence is not provided by the scanner's vendor (Philips), it was implemented through pulse programming by modifying the standard implementation of the multi-echo FFE with EPI readout. Pulse programming is a powerful tool for developing custom pulse sequences and modifying the MR scanner software. Through the Paradise Pulse Programming Environment (Pulse Programming Environment (PPE)), the programmer has access to the source code, written in Gyroscan Object-Oriented Acquisition Language (GOAL-C++). In GOAL-C++, basic elements of a pulse sequence, such as gradients or RF pulses, are modeled as objects. This allows the programmer to add or remove sequence elements and manipulate them by changing object attribute values. The following listing comprises a pseudocode to exemplify the attribute assignment of a gradient object:

the code modifications will only run if the new user variable is set to TRUE

new user variable of type yes or no

```
if (VAL01_ACQ->yn_add_new_grad == YES)  {

    float grad_strength = compute_grad_strength();

    GR:: new_grad->str = grad_strength

    float grad_slope = VAL01_ACQ->slope_duration_previously_defined;
    GR:: new_grad->slope = grad_slope

}
```

gradient strength assignment

gradient slope assignment

Listing 2.1: GOAL-C++ pseudocode for attribute assignment of a new gradient object

To test modified source code, the programmer can create a patch that loads new executable files instead of the product files during the startup of the acquisition software.

In this work, phantom imaging was performed before *in-vivo* scans to validate the developed sequence and to optimize the imaging parameters. Medical imaging phantoms are often used in MRI research for three reasons: First, they provide reliable reference measurements for qMRI, since their structure is known; Second, they enable the reproducibility of experiments using the same or different scanners because, unlike the human body, its properties do not change over time; third, phantom can also be useful for calibrating MRI systems [33].

Figure 2.1 summarizes the workflow pipeline followed to test and validate the sequence, as previously explained.

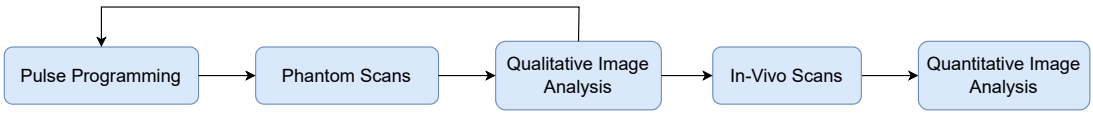

Figure 2.1: Workflow pipeline followed to test and validate the GESE sequence.

2.2 GESE Sequence Design

As mentioned in the previous section, the standard implementation of the FFE sequence was the starting point for achieving the GESE sequence. The FFE sequence consisted of a 90° excitation pulse with sinc profile, five-echo single-shot EPI readouts, and a Spectral Presaturation with Inversion Recovery

(SPIR) fat suppression pulse. The FFE sequence schematics generated by the Philips' Graphical Viewer Environment (GVE) can be seen in Figure 2.2(a).

The modifications performed in the product implementation included the addition of a refocusing pulse between the second and third echoes, three slice selection gradients, two phase-encoding gradients, and two frequency encoding gradients, which will be further explained below. All these added elements increased the duration of the sequence by seven milliseconds. Additionally, one phase encoding gradient was removed. For debugging purposes and to test different combinations of sequence elements, the implementation allows the user to selectively choose which elements to include. The final implementation of the GESE sequence is shown in Figure 2.3, in which all modifications performed are colored.

The GESE sequence employs a SPIR fat suppression pulse followed by a 90°excitation pulse, with a sinc shape for both pulses (4^{th} row in Figure 2.3). As explained in section 1.1, its purpose consists of forcing the nutation of the net magnetization vector from the longitudinal to the transverse plane, where the signal can be measured. After two echo acquisitions, a refocusing pulse is applied, which can be, according to user preference, a 180y simple pulse or a 90y240x90y composite pulse, both with block shape. Refocusing pulses negate spin dephasing effects caused by fixed external magnetic field inhomogeneities, including spoiler gradients such as the left crusher slice selection gradient. The spin-echo occurs when these dephasing effects cancel out, at

$$\mathrm{TE_{SE}} = 2 * \Delta t_{\text{90-180}}, \tag{2.1}$$

where Δt$_{\text{90-180}}$ is the time between the excitation and refocusing pulses.

However, as shown in Figure 2.3, in the current implementation, the TE$_{\text{SE}}$ occurs between the acquisition fourth and fifth echo and is not centered with any acquisition window.

To restrict the excitation to the spins of interest, a slice selection gradient is played simultaneously with the excitation pulse, followed by a slice rephasing gradient. Then, between the second and third echoes, one slice selection gradient surrounded by two crusher gradients is centered around the refocusing pulse. After all the echoes are acquired, a spoiler gradient is played.

As for the phase and frequency gradients, the standard EPI gradient lobes and blips are used to read the k-space of each echo. Between the second and third echoes, one phase encoding and one frequency encoding gradient blips are played before the refocusing pulse to force the k-space trajectory into the center of the k-space. After that, another phase and frequency gradient blips are played to place the k-space trajectory in k$_{\text{x,min}}$, k$_{\text{y,min}}$. After all the echoes are acquired, two spoiler gradients in the phase and frequency directions are employed.

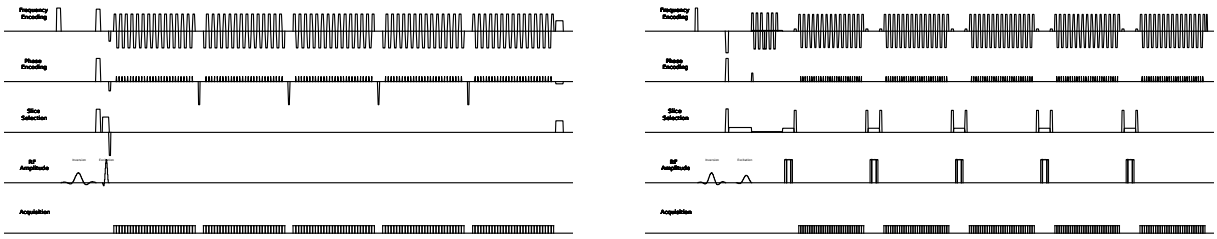

(a) (b)

Figure 2.2: Sequence schematics of the five-echo **(a)** FFE and **(b)** SE with EPI readout generated by the Philips' GVE.

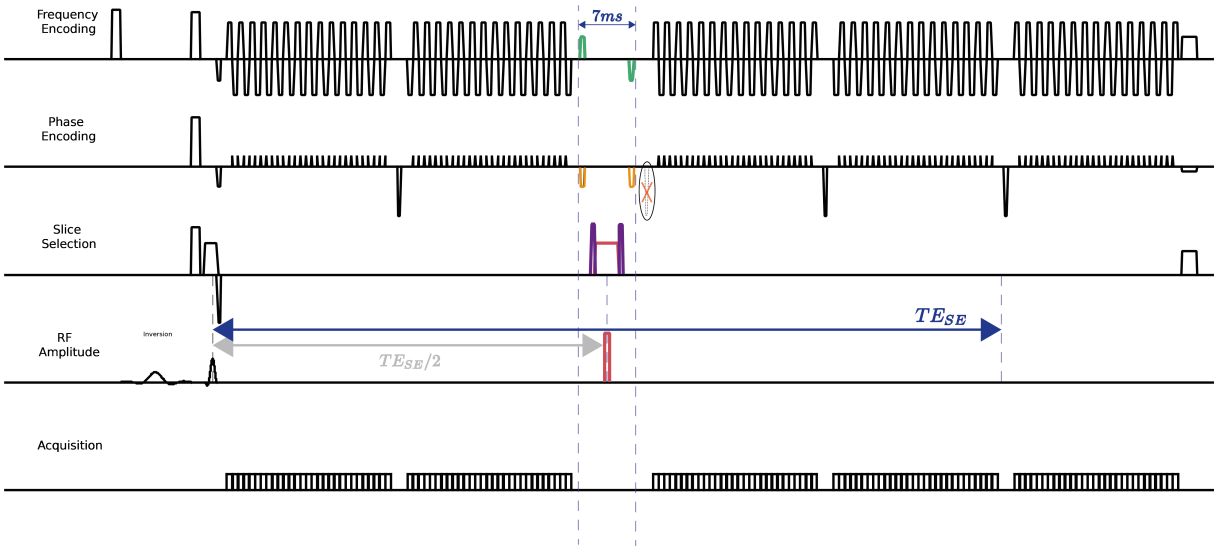

Figure 2.3: Sequence schematics of the five-echo GESE with EPI readout obtained through modifications performed to the standard implementation of the multi-echo FFE. The modifications include the addition of two frequency gradient blips (green), two phase gradient blips (yellow), two crusher gradients (purple), and a slice selection gradient and refocusing pulse (red). The yellow cross represents the removal of the first prephasing gradient along the phase encoding direction of the third echo acquisition. The added elements increased the sequence duration by 7 ms. The schematic was generated by the Philips' GVE.

2.3 Image Acquisition

All scans acquired in this work, presented in section 3, were performed on a 3.0T scanner (Ingenia, Philips, Best, The Netherlands). The proposed GESE sequence was compared against a five-echo FFE and SE sequences. The obtained T_2 and T_2^* maps generated with the proposed GESE sequence were compared with T_2 and T_2^* maps obtained with reference sequences. The sequences used as reference for T_2* and T_2 mapping mentioned in subsections 2.3.1 and 2.3.2.B are the standard implementations provided by the scanner's vendor with relatively short acquisition times.

2.3.1 Phantom

Phantom imaging was performed using the International Society for Magnetic Resonance in Medicine (ISMRM)/National Institute of Standards and Technology (NIST) system phantom. The phantom consists of three layers of sphere arrays aimed for different qMRI sequences. In this work, only the middle layer was scanned, since it has a range of different T_2 values (Figure 2.4). This layer has 14 spheres filled with $MnCl_2$ doped water and each sphere has a different standardized T_2 value ranging from approximately 6 to 581 ms (at 3T) [10, 34].

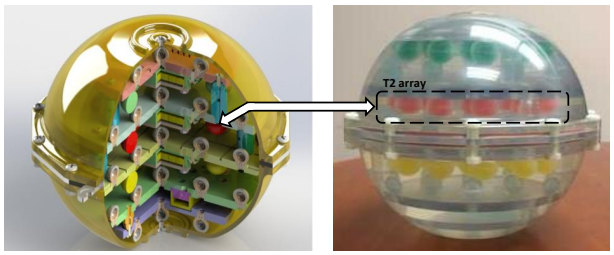

Figure 2.4: ISMRM/NIST system phantom composed of three layers with sphere arrays filled with different concentrations of $NiCl_2$, $MnCl_2$ and H_2O, resulting in different values of T_1, T_2 and proton density. For this study only the T_2 layer was used. Adapted from [10, 11]

A 15 channel head coil was used for the phantom experiments. For all scans a single slice was selected with coronal orientation with the following imaging parameters: FOV = 270 × 270 mm^2, in-plane resolution = 3 × 3 mm, and slice thickness = 4 mm. The TE for GESE, FFE, SE was set to the shortest value, of 10 ms , and TR was set to 10000 ms, to allow for recovery of the longitudinal magnetization. All sequences, with the exception of the T_2 Reference sequence, were tested with SPIR fat suppression pulse. Additional imaging parameters are specified in Table 2.1. The proposed GESE sequence was tested with 2 different refocusing pulses: a 180y simple pulse or a 90y240x90y composite pulse.

Table 2.1: Imaging parameters used for the phantom experiments.

Imaging Parameters	GESE | FFE | SE	Ref. T_2*	Ref. T_2
Technique	-	FFE	SE
Nº of echoes	5	20	9
Fast Imaging mode	EPI	-	GRASE (Turbo Spin-Echo (TSE)+EPI)
Factor	EPI factor = 29	-	TSE factor = EPI factor = 9
Shot mode	single-shot	-	multi-shot
SENSE factor	3	3	-
TE [ms]	10	1.19	7.9
ΔTE [ms]	19.4	1.5	-
FA	90°	50°	90° | 180°
TR [ms]	10 000	600	1 000
Partial Fourier (Halfscan)	no	0.6	no

2.3.2 In-Vivo

Two healthy subjects were scanned: one for brain imaging, and the other for cardiac acquisitions.

2.3.2.A Brain

The 15 channel head coil used in the phantom scans was also used for the brain scans. The sequences tested on the human brain were the proposed 2D five-echo GESE, FFE and SE. Due to time constraints, no Reference T_2* or T_2 mapping sequences were acquired. A single-slice was in transverse orientation was selected with: FOV = 230 × 230 mm^2, in-plane resolution of 2 × 2 mm, and slice thickness = 3 mm, EPI factor = 39, SENSE factor = 3 and with a SPIR fat suppresion pulse. Additional acquisition parameters are shown in Table 2.2.

Table 2.2: Imaging parameters used for the brain experiments.

Imaging Parameters	GESE | FFE | SE
Fast Imaging mode	EPI
Shot mode	single-shot
Nº of echoes	5
TE [ms]	14 (GESE and FFE); 31 (SE)
ΔTE [ms]	27.4
FA	90°
TR [ms]	3 000
Halfscan	no

2.3.2.B Heart

Cardiac scans were performed using a 16-channel anterior coil and a 12-channel posterior coil. For all scans, a single slice was selected in the short axis plane (see Figure 2.5). This view of the heart allows the comparison of the sizes of the left and right ventricles and the assessment of the left ventricular size, wall thickness, and systolic function.

The five-echo GESE, FFE, SE, as well as, the Reference T_2* sequence and T_2 mapping sequences were acquired with the acquisition parameters shown in Table 2.3. For GESE, FFE and SE, a Spectrally Selective Attenuated Inversion Recovery (SPAIR) fat supression pulse was selected. Additionally, for the Reference T_2* and T_2 mapping sequence, a black-blood prepulse was selected. All scans were set with a trigger delay of end diastole (903 ms) to minimize the cardiac motion.

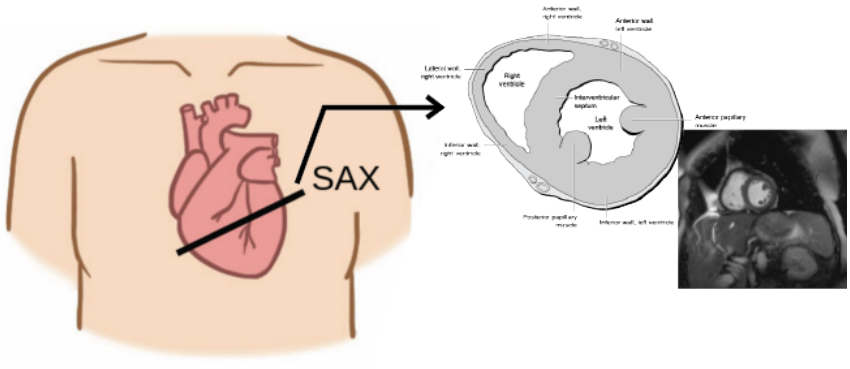

Figure 2.5: Short axis view of the heart with a clear depiction of the left and right ventricles. Adapted from [12–14]

Table 2.3: Imaging parameters used for the heart experiments.

Imaging Parameters	GESE | FFE | SE	T_2* ref	T_2 ref
Technique	-	FFE	SE
FOV [mm^2]	240 × 279	300 × 300	300 × 300
In-plane resolution [mm]	3.1 × 3.1	3.6 × 3.6	3.1 × 3.1
Slice thickness [mm]	8	10	8
Fast Imaging mode	EPI	Turbo Field Echo (TFE)	GRASE (TSE + EPI)
Factor	EPI factor = 31	8	TSE factor = 9 | EPI factor = 7
Shot mode	single-shot	multi-shot	multi-shot
Nº of echoes	5	15	9
TE [ms]	10	0.97	7.4
ΔTE [ms]	19.1	0.9	-
FA	90°	25°	90° | 180°
TR [ms]	1 200 (1 beat)	15	1 200 (1 beat)
SENSE factor	3	2	2

2.4 Image Post-Processing

All post-processing steps were carried out in Matlab R2021a using original scripts unless mentioned otherwise. Starting from the scanner data extraction, the data relative to each scan was extracted in the Digital Imaging and Communications in Medicine (DICOM) format. DICOM files store not only the raw images but also information related to the acquisition parameters in a single complex structure. For quantitative analysis, raw pixel values should not be used as they are integers, instead each pixel should be scaled according to: I = slope ×SV + intercept, where SV is the raw stored value and I is the "true" transformed pixel intensity.

The reference T_2* and T_2 maps were generated inline by the scanner and the GESE T_2* and T_2 maps were computed offline using a 4-parameter [15] pixel-by-pixel least squares fit, as follows:

$$S(\tau) = \begin{cases} S_0^I \cdot e^{-\tau \cdot R_2^*} & , 0 < \tau < TE_{\text{SE}}/2 \\ S_0^{II} \cdot e^{TE_{SE} \cdot (R_2^* - R_2)} \cdot e^{-\tau \cdot (2 \cdot R_2 - R_2^*)} & , TE_{\text{SE}}/2 < \tau < TE_{\text{SE}} \end{cases} \tag{2.2}$$

where S_0^{I} and S_0^{II} are the equilibrium signals before and after the refocusing pulse, respectively, τ is the echo time and TE_{SE} is the time at which the spin-echo occurs.

For the phantom experiments, circular masks were created and mean T_2 and T_2^* values for each vial were computed. Correlation and Bland-Altman plots were performed using the values obtained with the

proposed five-echo GESE and the proposed Reference sequence.

For the in-vivo scans, individual masks were computed for each sequence presented, to avoid incorrect Region Of Interest (ROI) positioning due to volunteer motion. The left-ventricular (heart) and white- and gray-matter (brain) masks were manually drawn using an in-house developed MATLAB script.

3

Results

3.1 Phantoms

3.1.1 Sequence Development

This section is intended to show the image evolution of echoes three to five throughout the modifications performed to the scanner vendor's implementation of the 2D five-echo FFE sequence with single-shot EPI readout, from the addition of a refocusing pulse to the final sequence (see subsection 2.3.1 for further information regarding imaging parameters).

Starting from Figure 3.1(a), a simple refocusing pulse, set with block shape and a FA of 180°, was added between the acquisitions of the second and third echoes. In addition, the first prephasing gradient along the phase encoding direction of the third acquisition was removed, as the refocusing pulse negates the phase of the spins. Figure 3.1(b) shows that the first two echo acquisitions, which were not submitted to sequence modifications, are faithful T_2*-weighted phantom images but, from the third to fifth echoes, images present several artifacts. This was expected since no slice has been selected for refocusing, thus, each image from the third echo onward consists of the sum of the signals from all spins along the

slice selection direction.

Following this, a slice selection gradient was placed simultaneously with the refocusing pulse, as can be seen in Figure 3.2(a), and then a crusher pair was added, as can be observed in 3.3(a). Figures 3.2(b) and 3.3(b) present severe signal loss, which makes the task of visual inspection almost impossible.

The image signal was recovered in Figure 3.4(b) due to the addition of two pairs of phase and frequency gradient blips placed before and after the refocusing pulse (3.4(a)), with an area equal to the first frequency and phase prephasing gradients of the first EPI readout. The gradient blips placed before the pulse force the k-space trajectory into the center of k-space and the gradient blips placed after the pulse move the k-space trajectory back to $k_{x,min}$, $k_{y,min}$ to allow the start of another EPI k-space readout.

The last modification to the proposed GESE sequence is depicted in Figure 3.5(a) and it consists of the increase in strength and duration of the slice selection gradient. The strength of the added slice selection gradient matches the strength of the first slice selection gradient, which is applied during slice excitation, and its duration was chosen experimentally throughout the UI parameter created to test several duration values. The improvements in the slice selection gradient resulted in an increase in signal amplitude in the last three echoes.

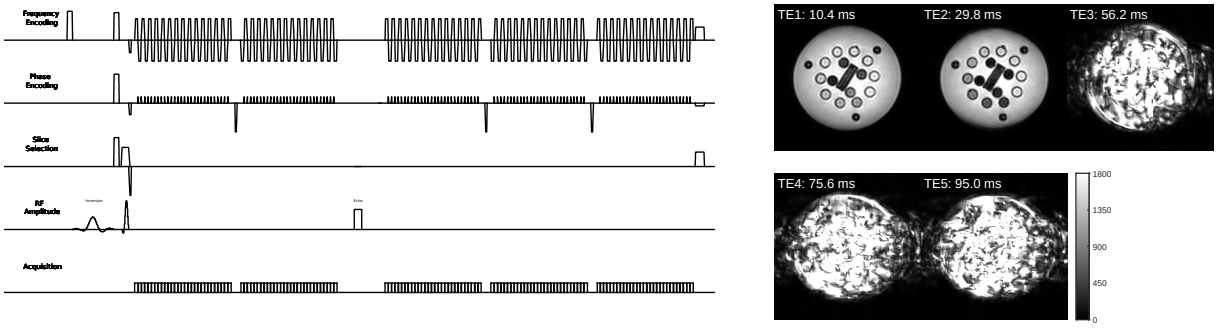

(a) **(b)**

Figure 3.1: (a) Sequence diagram of the five echo implemented GESE sequence with a 180° RF pulse added between the second and third echoes. **(b)** Phantom images acquired from the sequence shown in (a) with echo times specified on the top left corner of each image. All images are displayed with the same scale of image intensity in arbitrary units (a.u.).

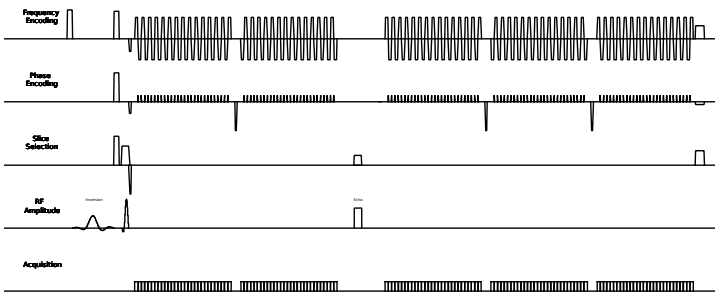

(a) Figure A

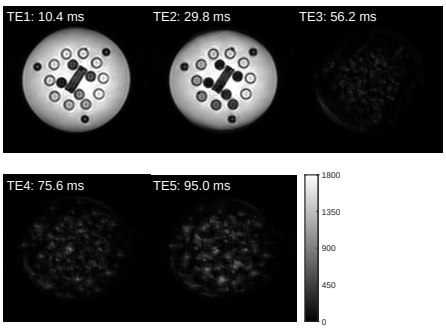

(b) Figure B

Figure 3.2: (a) Sequence diagram of the five echo implemented GESE sequence with a 180° RF pulse and a slice selection gradient added between the second and third echoes. **(b)** Phantom images acquired from the sequence shown in (a) with echo times specified on the top left corner of each image. All images are displayed with the same scale of image intensity in arbitrary units (a.u.).

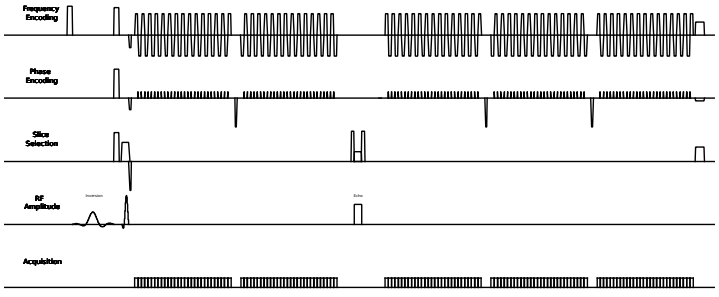

(a) Figure A

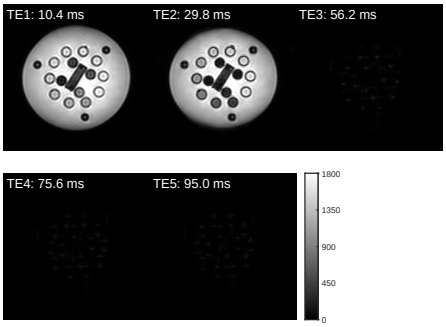

(b) Figure B

Figure 3.3: (a) Sequence diagram of the five echo implemented GESE sequence with a 180° RF pulse, a slice selection gradient and a crusher pair added between the second and third echoes. **(b)** Phantom images acquired from the sequence shown in (a) with echo times specified on the top left corner of each image. All images are displayed with the same scale of signal amplitude in arbitrary units (a.u.).

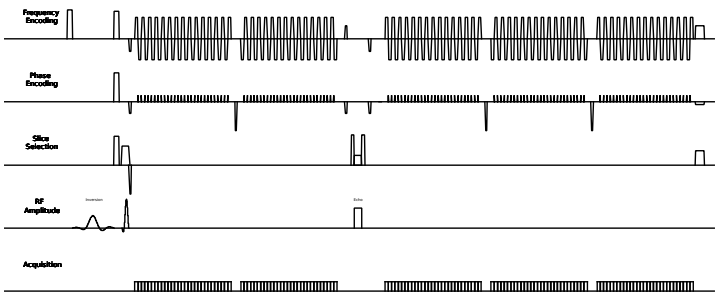

(a) Figure A

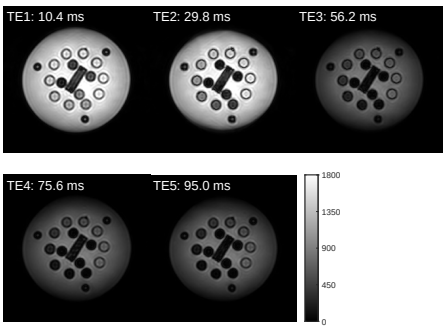

(b) Figure B

Figure 3.4: (a) Sequence diagram of the five echo implemented GESE sequence with a 180° RF pulse, a slice selection gradient, a crusher pair and two pairs of phase and frequency gradient blips added between the second and third echoes. **(b)** Phantom images acquired from the sequence shown in (a) with echo times specified on the top left corner of each image. All images are displayed with the same scale of signal amplitude in arbitrary units (a.u.).

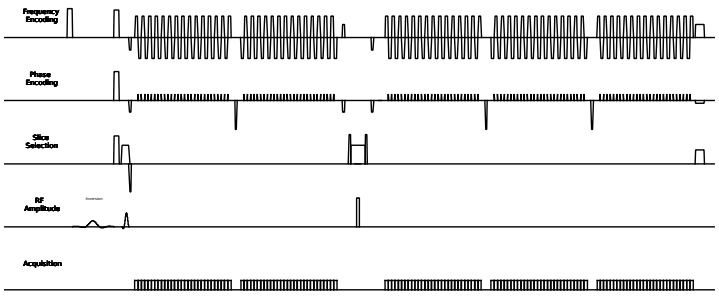

(a) Figure A

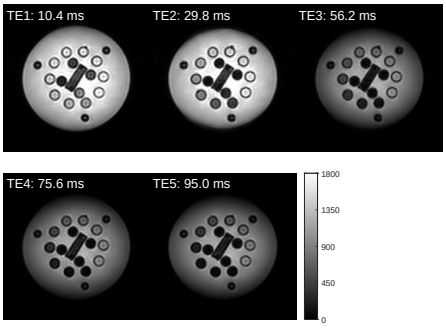

(b) Figure B

Figure 3.5: (a) Sequence diagram of the five echo implemented GESE sequence with a 180° RF pulse, a slice selection gradient, a crusher pair and two pairs of phase and frequency gradient blips added between the second and third echoes. In this case, the slice selection gradient has increased strength and duration than in the previous cases. **(b)** Phantom images acquired from the sequence shown in (a) with echo times specified on the top left corner of each image. All images are displayed with the same scale of signal amplitude in arbitrary units (a.u.).

Figure 3.6(a) contains the five-echo images generated with the implemented GESE sequence. From the third echo, the images acquired from the vendor's FFE show artifacts in the edges of the phantom and small phantom spheres which are related to signal loss due to T_2* decay. Figures 3.6(b) and 3.6(c) depict the images acquired with the proposed GESE sequence with simple and composite pulses, respectively. As expected, the artifacts are greatly reduced, as the 180° RF pulse reduces spin dephasing due to magnetic field inhomogeneities.

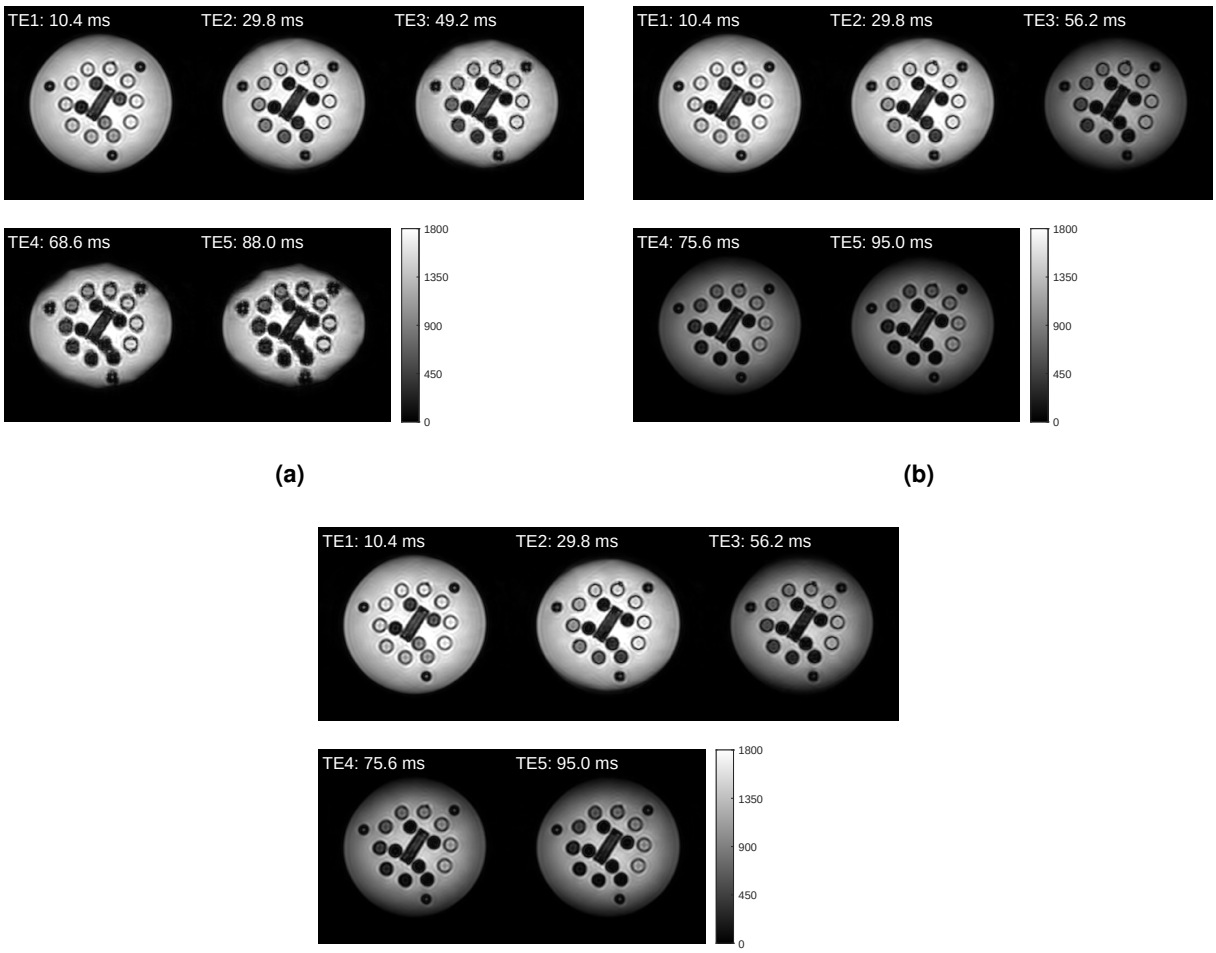

Figure 3.6: **(a)** Five-echo acquisition with the vendor's FFE sequence set to a 90 ° FA with single-shot EPI readout, coronal slice orientation, FOV=270×270mm, slice thickness = 4mm, voxel size = 3x3 and SENSE reduction factor = 3. **(b)** Five-echo acquisition of the new sequence generated from (a) with the addition of a simple 180° refocusing pulse between echoes two and three, a slice selection gradient surrounded by a crusher pair, two frequency gradient lobes and two phase gradient lobes. Echo times are specified on the top left corner of each image. **(c)** Five-echo acquisition of the sequence described in (b) with a composite refocusing pulse. All images are displayed with the same scale of image intensity in arbitrary units (a.u.).

3.1.2 Sequence Validation

To evaluate the performance of the GESE sequence, several experiments were conducted on the NIST phantom. Figure 3.8, shows the signal evolution over five echoes of the Gradient-Echo, the GESE sequence with simple and composite refocusing pulses. Each plot displays mean signal with the corresponding ROIs, represented in Figure 3.7. Each ROI has a circular shape and was centered inside the sphere of interest. Additionally, the standard deviation inside of each ROI is also displayed in Figure 3.8

for each echo.

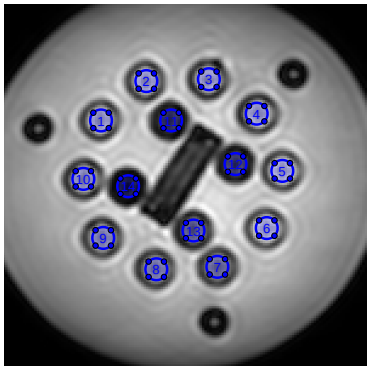

Figure 3.7: Representation of the fourteen ROIs selected for signal measuring within the NIST phantom. The ROIs coincide with the fourteen phantom spheres.

Figure 3.9(a) and 3.9(b) contain the T_2* maps obtained with the reference and with the proposed GESE sequence, respectively. Figure 3.10(a) and 3.10(b) shows the T_2 maps computed using the reference and the proposed GESE sequence, respectively.

To assess the accuracy of T_2* and T_2 parameter estimation using the GESE sequence with composite pulse, T_2* (Figure 3.9(b)) and T_2 (Figure 3.10(b)) maps were computed and compared with scanner generated T_2* and T_2 maps acquired with standard vendor sequences used as reference, shown in Figures 3.9(a) and 3.10(a).

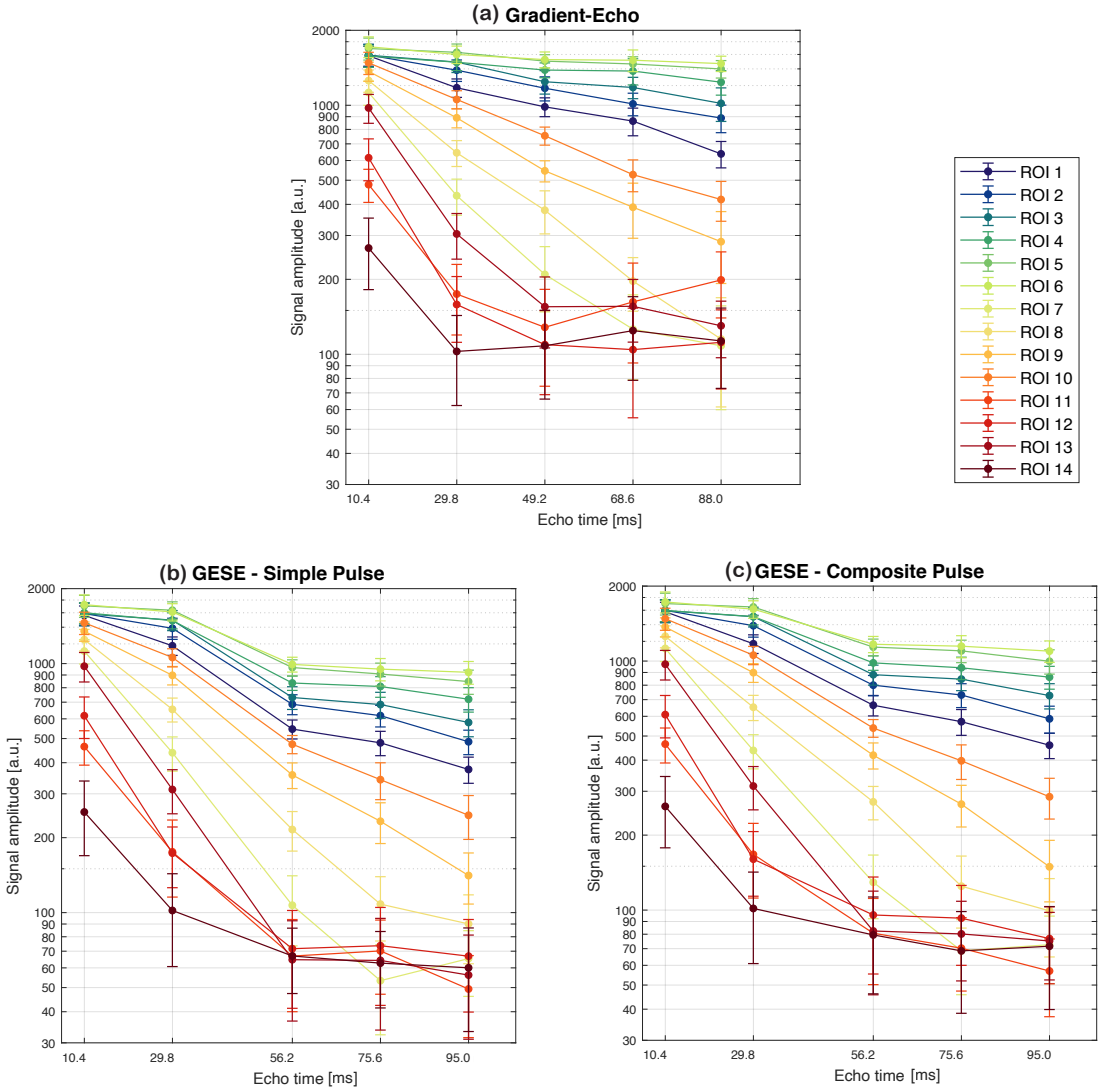

Figure 3.8: Mean signal evolution over five echoes of the **(a)** Gradient-Echo, **(b)** GESE with simple pulse and **(c)** GESE with composite pulse sequences for the fourteen phantom ROIs. The bars indicate the standard deviation of the measured signals. For improved visualization, a logarithmic scale was used in the vertical axis.

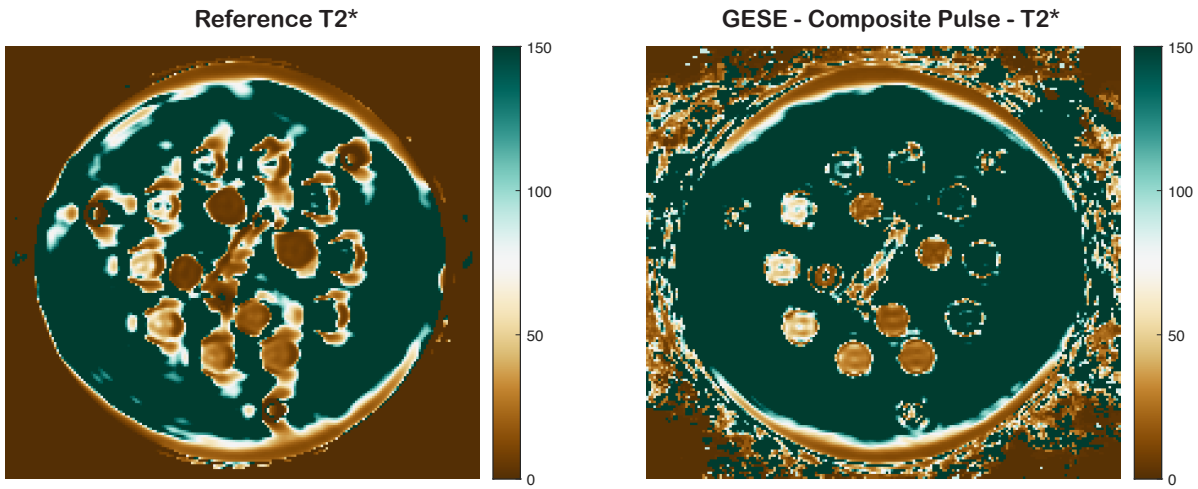

Figure 3.9: T_2* maps computed from the **(a)** Reference T_2* sequence and **(b)** GESE with composite pulse sequence for the phantom.

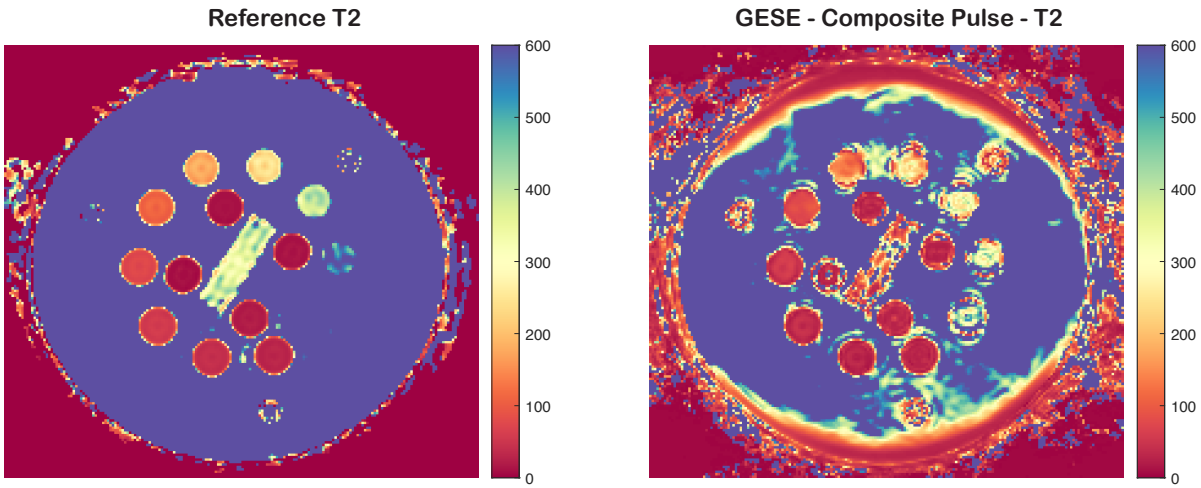

Figure 3.10: T_2 maps computed from the **(a)** Reference T_2 sequence and **(b)** GESE with composite pulse sequence for the phantom.

From the maps of the GESE, Reference T_2* and Reference T_2 sequences, mean values for T_2* and T_2 inside each of the fourteen ROIs, previously shown in Figure 3.7, were computed. The values obtained are represented in the format of correlation plots, in Figures 3.11(a) and 3.12(a), for ease of

comparison. Some outlier points, that correspond to phantom spheres with higher values of T_2* and T_2, were excluded from this analysis, as they are not expected to be seen in-vivo. For outlier exclusion, a threshold of T_2* $>$ 100 ms and $T_2 >$ 200 ms was established. The variable ”n” displayed in the correlation plots represents the number of ROIs taken into account.

Correlation plots are a useful tool for inspecting for a linear relationship between a certain variable, in this case, either T_2* or T_2, obtained with different techniques, such as the sequence in the study versus a reference sequence. The squared Pearson correlation coefficient - r^2 - is a measure that indicates how close the data points are to the predicted linear fit equation, i.e., if there is a strong linear association between both variables. The value of r^2 ranges between -1 and 1, where a value of 0 corresponds to no correlation, -1 corresponds to a good linear fit with a negative slope and 1 corresponds to a good linear fit with a positive slope. In this case, the ideal situation would be a linear fit equation with a slope of 1 and an intercept of 0, and an r^2 of 1, which would indicate that both sequences produced the same results and are perfectly correlated.

For further statistical analysis, Bland-Altman plots were also computed for T_2* and T_2 and are shown in Figures 3.11(b) and 3.12(b), respectively. Bland-Altman plots, like correlation plots, are also useful to evaluate two measurement techniques [35, 36]. For this case in particular, the x axis corresponds to the mean of T_2* or T_2 measured with GESE and the correspondent Reference sequence and the y axis corresponds to the difference of these variables. This plot displays the bias, which is the mean of differences, and the two limits of agreement (upper and lower), which is given by the bias ±1.96 Standard Deviation (SD) of the differences.

Starting with T_2* measurement analysis, 8 ROIs were taken into account in a linear fit with slope of 0.79 and intercept of 8.64 with an r^2 of 0.96. For T_2, 9 ROIs were taken into account in a linear fit with slope of 0.62 and intercept of 14.8 with an r^2 of 0.95.

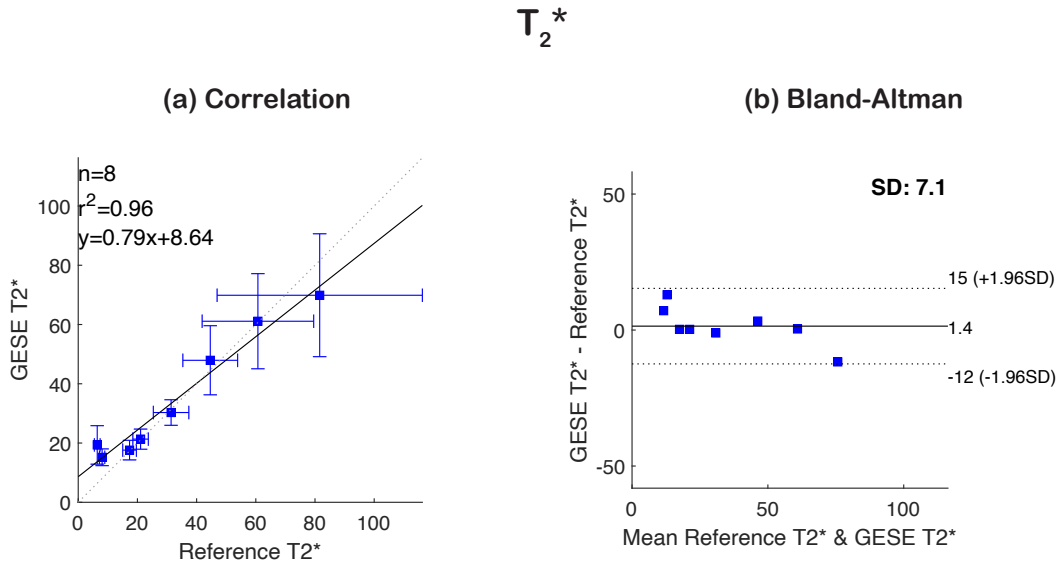

Figure 3.11: **(a)** Correlation and **(b)** Bland-Altman plots comparing the mean T_2* values obtained with the Reference T_2* and GESE with composite pulse sequences. Only nine out of the fourteen ROIs were considered.

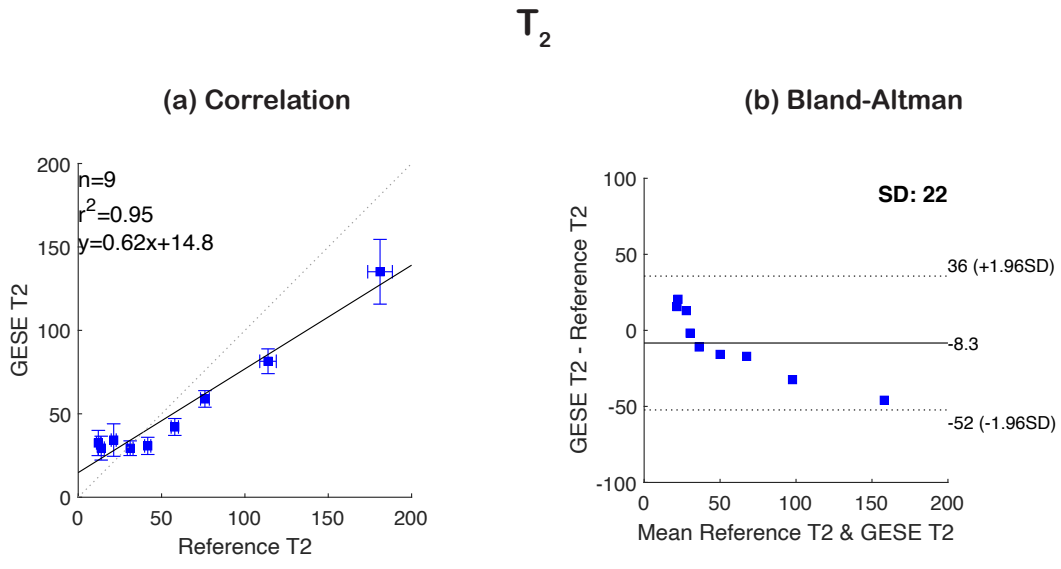

Figure 3.12: **(a)** Correlation and **(b)** Bland-Altman plots comparing the mean T_2 values obtained with the Reference T_2 and GESE with composite pulse sequences. Only thirteen out of the fourteen ROIs were considered.

3.2 Volunteers

3.2.1 Brain

For the analysis of the brain scans, two ROIs with circular shape were selected, white matter (ROI 1) and grey matter (ROI 2) regions. The ROIs are represented in Figure 3.13. Figure 3.14 contain the plot with the signal amplitude, per echo time, extracted for the measured signal inside both ROIs for the different sequences.

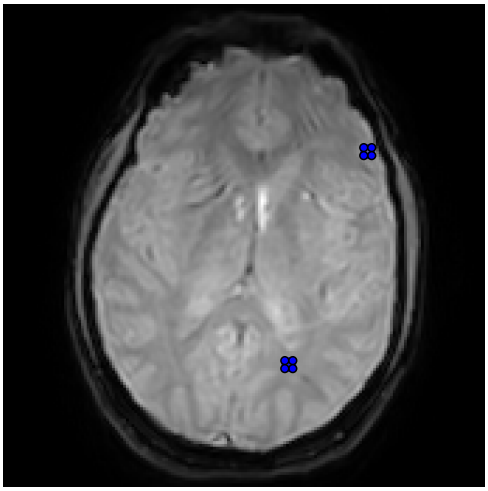

Figure 3.13: Representation of the two ROIs selected for analysis from the brain scans. One ROI corresponds to a grey matter region and the other corresponds to a white matter region.

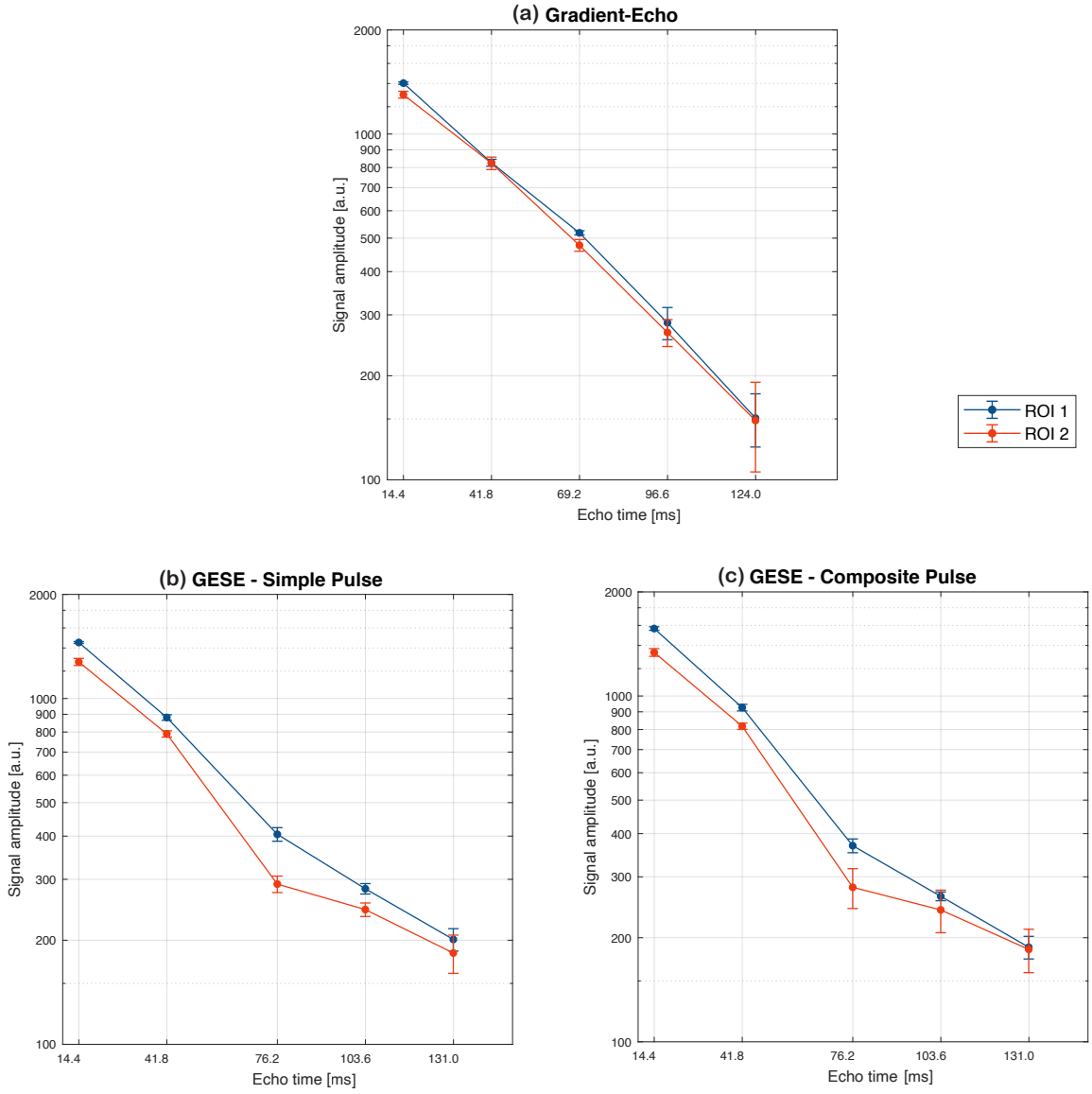

Figure 3.14: Mean signal evolution over five echoes of the **(a)** Gradient-Echo, **(b)** GESE with simple pulse and **(c)** GESE with composite pulse sequences for the two brain ROIs. The bars indicate the standard deviation of the measured signals.

T_2* and T_2 maps were computed from the scans obtained with the GESE sequence with both simple and composite pulses (for simplification, only the maps acquired with the composite pulse are shown, in Figures 3.15(a) and 3.15(b)), however, due to time restrictions, no reference T_2 and T_2^* mapping scans were acquired. Instead, the reported values will be compared against available literature. The mean

values for T_2* and T_2 inside both ROIs are shown on Table 3.1, as well as the values extracted from the literature.

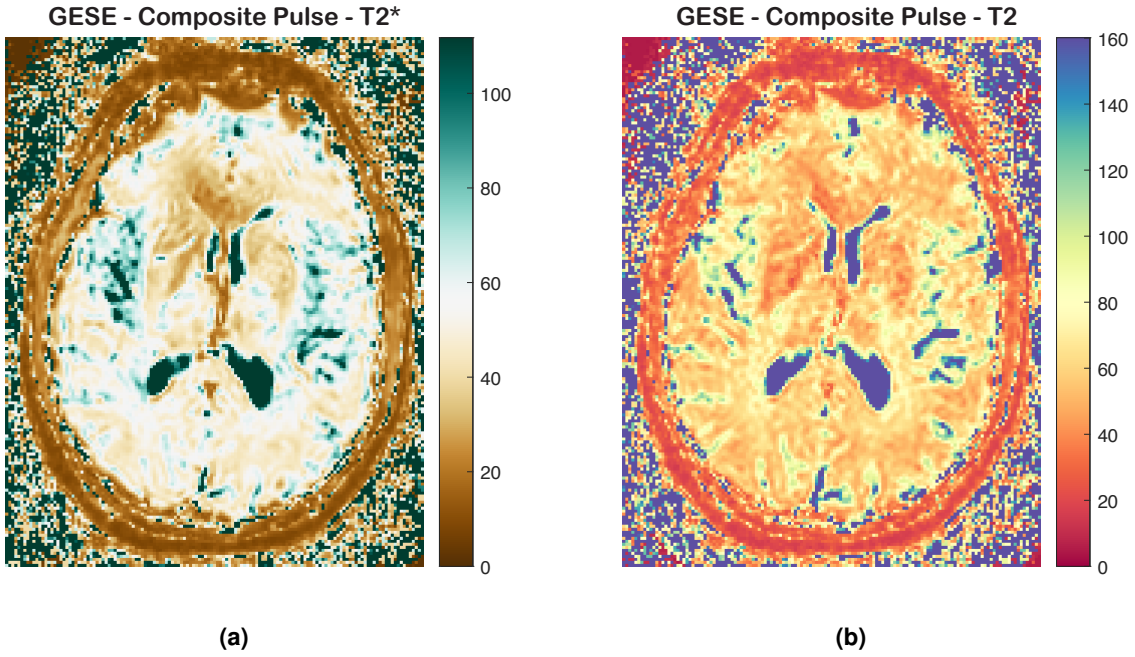

Figure 3.15: In vivo brain **(a)** T_2* and **(b)** T_2 maps computed from the GESE with composite pulse sequence.

Table 3.1: Mean T_2* and T_2 values measured for the two brain ROIs using the GESE with either simple or composite pulse.

Sequence	Tissue	T_2* (ms) mean ± SD	T_2 (ms) mean ± SD
GESE - Simple Pulse	White matter (ROI 1)	55 ± 1	64 ± 2
	Gray matter (ROI 2)	57 ± 2	78 ± 5
GESE - Composite Pulse	White matter (ROI 1)	52 ± 2	64 ± 4
	Gray matter (ROI 2)	56 ± 3	80 ± 8

3.2.2 Heart

For the analysis of the cardiac scans, a single ROI was chosen within the myocardium, represented in Figure 3.16. The signal amplitude inside the ROI against echo time is shown in Figure 3.17.

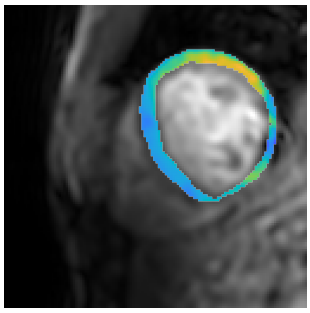

Figure 3.16: Representation of the ROI selected for analysis from the heart scans. The ROI corresponds to a region of the myocardium.

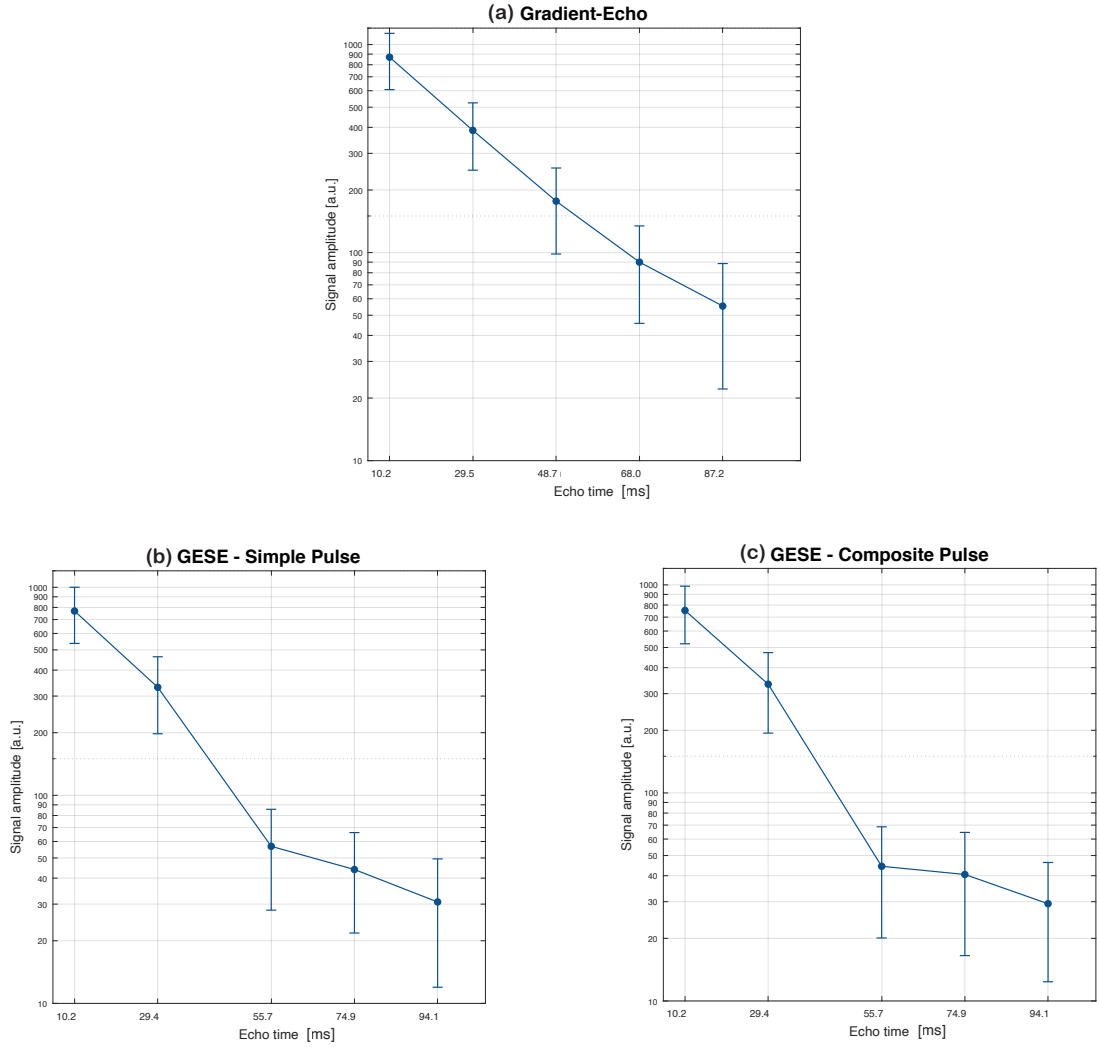

Figure 3.17: Mean signal evolution over five echoes of the **(a)** Gradient-Echo, **(b)** GESE with simple pulse and **(c)** GESE with composite pulse sequences of the heart ROI. The bars indicate the standard deviation of the measured signals.

The T_2* and T_2 maps retrieved from the GESE with composite pulse and the reference sequences are shown in Figures 3.18 and 3.19 and the extracted mean ROI values are shown in Table 3.2.

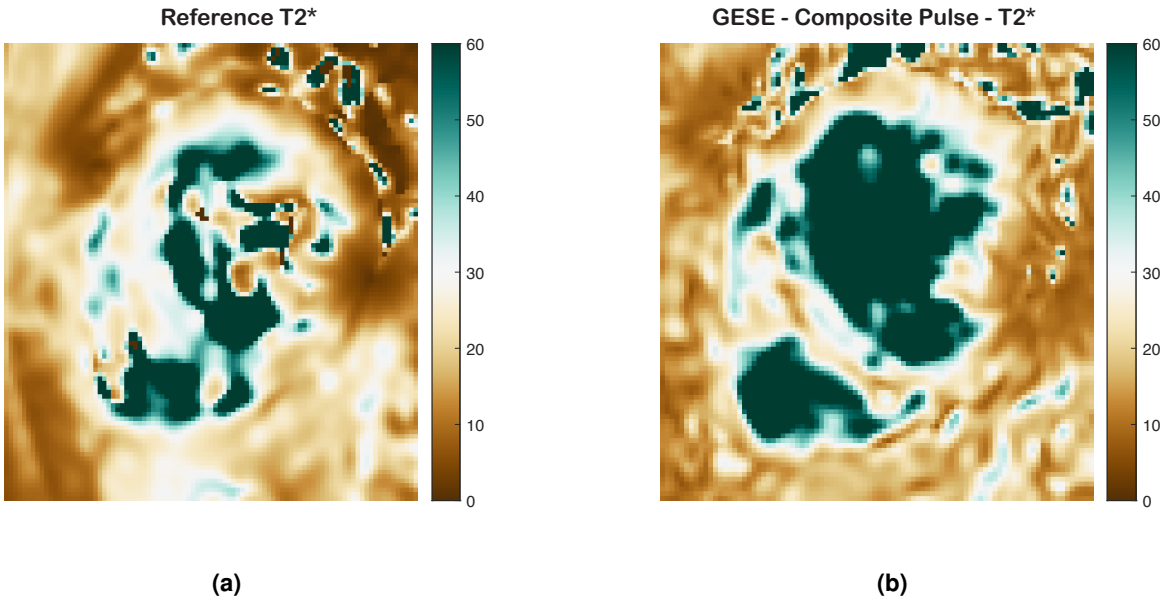

Figure 3.18: T_2* maps computed from the **(a)** Reference T_2* sequence and **(b)** GESE with composite pulse sequence for the heart.

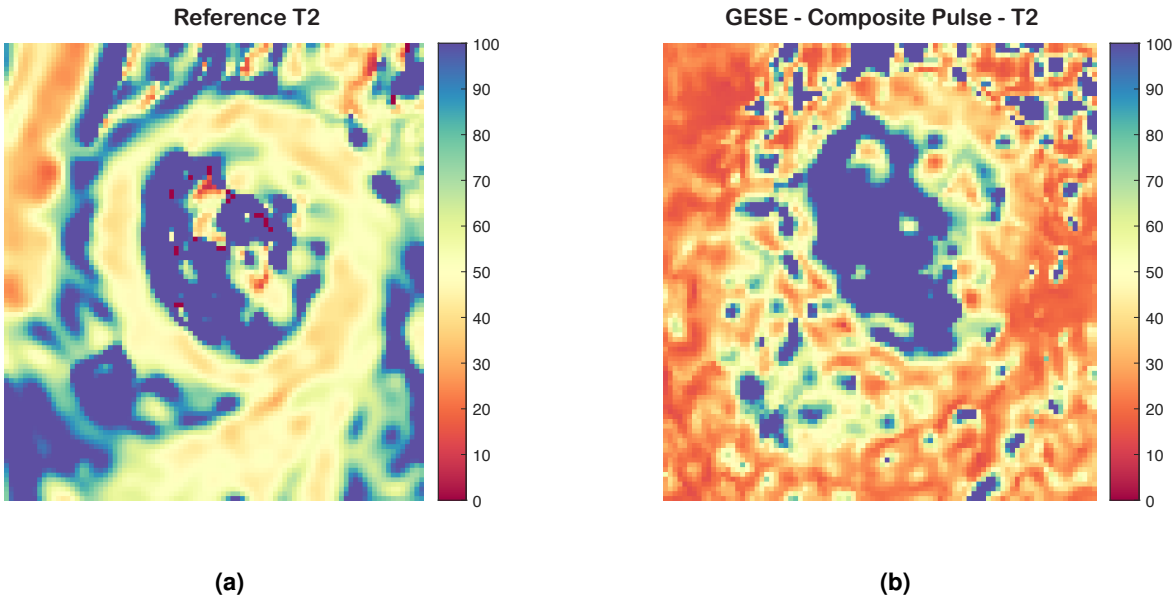

Figure 3.19: T_2 maps computed from the **(a)** Reference T_2 sequence and **(b)** GESE with composite pulse sequence for the heart.

Table 3.2: Mean T_2* and T_2 values measured measured for the heart ROI using the GESE with either simple or composite pulse.

Sequence	$\mathbf{T_2}$* (ms) mean $\pm$ SD	$\mathbf{T_2}$ (ms) mean $\pm$ SD
Reference	24 ± 9	47 ± 7
GESE - Simple Pulse	25 ± 10	34 ± 14
GESE - Composite Pulse	27 ± 12	46 ± 32

4

Discussion

4.1 Phantom

In Figures 3.6(a), 3.6(b) and 3.6(c) it is possible to observe a reduction in signal amplitude in images of echoes three to five acquired with GESE compared to the echo images from the vendor's FFE sequence. A possible cause for the signal loss that occurred after the refocusing pulse was applied could be the imperfect design of the crusher gradients or a slice profile mismatch between the excitation and refocusing. Furthermore, the images obtained with the GESE with a composite pulse showed slightly higher signal amplitude values for echoes three to five compared to the images obtained with the GESE with a simple pulse, which indicates that the composite pulse might have partially mitigated slice profile mismatch complications.

Regarding the plots of signal amplitude versus TE obtained for the phantom (Figure 3.8), for GE (Figure 3.8(a)) the signal from all ROIs decays throughout the echoes, as expected, except for ROIs 6, 11, 12 and 14. For ROI 14, the signal increases between echoes 2 to 3 and echoes 3 to 4; for ROI 6, the signal increases between echoes 3 to 4; for ROI 11, the signal increases between echoes 3 to 4 and 4 to 5; and for ROI 12, the signal increases between echoes 4 to 5. This was not expected to occur in a

GE sequence, however, because the mentioned ROIs correspond to the phantom spheres with smaller values of T_2* decay (except ROI 6), the irregularities of the signal evolutions detected might be due to image artifacts.

In the signal plots obtained for the GESE (Figure 3.8(b-c)) it is possible to observe a reduction in the signal amplitude of all ROIs between echoes 2 and 3, compared to the GE values. However, for the composite refocusing pulse (Figure 3.8(c)) this signal loss was more attenuated.This was expected considering the results obtained in Figures 3.6(a), 3.6(b) and 3.6(c). Additionally, for almost all ROIs, the signal decay rate decreased from the third echo, indicating that the refocusing pulse partially refocused some of the spin dephasing caused by local field inhomogeneities.

The phantom T_2* and T_2 maps (Figures 3.9(b) and 3.10(b)) obtained with the GESE sequence present more artifacts in the background than in the maps obtained with the Reference sequences. Because the latter ones were computed online by the scanner, they might have been submitted to more robust post-processing. By visual inspection it is possible to conclude that the T_2* maps obtained with the GESE sequence present fewer artifacts inside the phantom compared to the Reference T_2*. Regarding the T_2 maps, the opposite is verified. This was expected since the Reference T_2* sequence does not perform spin refocusing after spin excitation, and the Reference T_2 sequence employs several refocusing pulses.

The T_2* Correlation (Figure 3.11(a)) plot shows a correlation coefficient of 0.96, indicating a strong linear association between the T_2* obtained with GESE sequence and the T_2* obtained with Reference T_2* sequence. Five intermediate values, comprised roughly between a Reference T2* of 18 and 62 ms, are very close to the y=x equation (dashed line on the plot), which indicates strong proximity of values between both sequences. The SD is visibly higher for the phantom spheres with higher values of T_2* which indicates that the measurements are less reliable for high T_2* values. Regarding the T_2* Bland-Altman (Figure 3.11(b)) plot, all values are inside the limits of agreement. Additionally the low value of the bias confirms the good agreement between the two sequences.

For T_2 even though there is a strong linear association between the T_2 values obtained with the GESE sequence and those obtained with the Reference sequence, as supported by the r^2 value of 0.95, this does not translate into the desired trend of having identical T_2 values for both sequences. The obtained linear equation's slope of 0.62 and offset of 14.8 shows that it differs significantly from the ideal linear equation, whose slope would be 1 and offset would be 0.

The less satisfactory results obtained for T_2 might be related to some limitations inherent to the GESE sequence. Since only 3 echoes with short echo spacing are used to estimate T_2, GESE sequence has limited capacity to estimate higher values of T_2.

4.2 Brain

As expected from the phantom experiments, in Figure 3.14, there is a visible signal drop between the second and third echoes in the signal measured with the GESE sequence (Figure 3.14(b) and (c)) when compared to the GE sequence. Additionally, it is possible to observe a reduction in the signal relaxation rate after the third echo for in Figures 3.14(b) and (c) when compared to the GE sequence , which was also expected.

Table 4.1 shows the T_2* and T_2 obtained for WM and GM, as well as the values retrieved from literature.

Table 4.1: Comparison of T_2* and T_2 values of the brain reported in the literature using GESE and standard sequences for T_2* and T_2 quantification vs the values obtained in this work.

Sequence	T_2* (ms) mean ± SD		T_2 (ms) mean ± SD	
	White matter	Gray matter	White matter	Gray matter
Literature - Standard Sequences [24] [21]	44 ± 2	60 ± 3	75 ± 3	83 ± 4
Literature - GESE [16]	49	50	63	71
GESE - Simple Pulse	55 ± 1	57 ± 2	64 ± 2	78 ± 5
GESE - Composite Pulse	52 ± 2	56 ± 3	64 ± 4	80 ± 8

As it can be seen in Table 4.1, in general, the estimated values of T_2* and T_2 obtained with the GESE sequence were similar between the simple and composite pulse implementations.

Concerning the value retrieved in the white matter, T_2* measured with the GESE sequence with composite pulse estimation provided the best results, which were similar to the literature value using the same sequence (RE = 6.1%) and relatively distant from the value retrieved from literature using a standard sequence (RE = 19.5%). While for T_2, the values of GESE sequence with composite pulse and simple pulse matched and were considerably similar to the literature value using the same sequence (RE = 1.6%) and more distant from the value retrieved from literature using a standard sequence (RE = 14.7%)

For gray matter, the T_2* measured with the GESE sequence with composite pulse was closer to the literature value using the the same sequence (RE = 12%) and T_2* with the GESE sequence with simple pulse was very similar to the literature value using the standard sequences (RE = 4.8%) . As for T_2, the value measured with the GESE sequence with simple pulse was closer to the literature value using the same sequence (RE = 9%) and the value measured with the GESE sequence with composite pulse was very similar to the literature value using a standard sequence (RE = 3.6%).

After analysis of the results obtained for WM, it is possible to conclude that the GESE with composite pulse provided values of T_2* and T_2 were very similar to the values retrieved from literature using the same sequence, with relative errors of 6.1% and 1.6%, respectively. The values obtained deviated more

from the literature values using other standard quantification sequences.

The values obtained for GM generated higher relative errors when compared to literature using the same sequence. A possible cause might be related to inaccurate ROI positioning. However, the relative errors were reduced when compared to the values from literature using standard sequences.

4.3 Heart

Regarding the signal amplitude against TE plots obtained for the GE and the GESE on the myocardium (Figure 3.17), similarly to what was observed in the brain, there is a visible reduction in the signal relaxation rate from the third echo for Figures 3.17(b) and (c) when compared to the GE sequence.

Table 4.2 shows the T_2* and T_2 obtained for the myocardium, as well as the values retrieved from literature.

Table 4.2: Comparison of T_2* and T_2 values of the myocardium reported in the literature using GESE and standard sequences for T_2* and T_2 quantification vs the values obtained in this work.

Sequence	**T_2*** (ms) mean ± SD	**T_2** (ms) mean ± SD
Literature - Standard Sequences [23], [21]	24 ± 5	67 ± 5
Literature - GESE [15]	28 ± 5	43 ± 5
Reference Scans	24 ± 9	47 ± 7
GESE - Simple Pulse	25 ± 10	34 ± 14
GESE - Composite Pulse	27 ± 12	46 ± 32

For the T_2* values of the myocardium, the GESE with simple pulse provided better estimations when comparing to the Reference sequence and literature using a standard sequence (RE = 4.2 % for both), however the value from the GESE sequence with composite pulse was very similar to the value retrieved from the literature using the same sequence (RE = 1.8 %). For the T_2, the GESE with composite pulse provided better results when compared to all values retrieved from literature (RE = 6 % for literature using GESE and RE = 31.3% for literature using a standard sequence) and reference sequence (RE = 2.1%).

After a more detailed inspection of the results obtained for the myocardium, it is possible to conclude that the GESE sequence with composite pulse provided values of T_2* and T_2 very similar to the values retrieved from literature using the same sequence, with relative errors of 1.8% and 6%, respectively.

5

Conclusion and Future Work

From the in vivo experiments performed with the proposed GESE sequence, a visible reduction in the ROI signal relaxation rate was observed for the echoes acquired after the refocusing pulse, showing that the refocusing pulse partially refocused the spin dephasing caused by local field inhomogeneities. However, it is likely that imperfect crusher gradients design compromised the signal amplitude of the last acquired echoes. Between the two pulses tested, simple and composite, the composite pulse provided more satisfactory results.

In general, for the myocardium and white matter, the values of T_2* and T_2 using the GESE with composite pulse were similar to the ones reported in literature using the same sequence and generated relative errors between 1.6 and 6.1%. For gray matter, the T_2* and T_2 values were more distant from to the ones reported in literature using the GESE sequence, with relative errors of 12.0% and 12.7%, respectively. A possible cause for the less satisfactory results in GM might be inaccurate ROI positioning.

Several limiting factors affected the results obtained, such as the reduced number of volunteers tested, which limits the comparison of the T_2* and T_2 values obtained with the GESE sequence versus the values retrieved from the literature. In addition, the limited number of echoes acquired limits the accuracy of the least-squares fit performed to obtain the quantitative maps. However, acquiring a higher

number of echoes would compromise temporal resolution which could be a downside for applications where a temporal resolution is desired, such as CMR. Furthermore, the definition of ROIs was performed manually; therefore, a more robust technique should be used, such as automatic tissue segmentation, for a more precise selection of ROIs. In addition, because the TE_{SE} is not centered with any acquisition window, none of the echo images acquired is only T_2-weighted.

Further sequence optimization steps should be taken to improve the accuracy of T_2* and T_2 quantification using the developed sequence. First, TE_{SE} should be centered on the fifth acquisition window. This can be done by increasing the time interval between the second echo acquisition and the refocusing pulse. Second, different values of echo spacings (ΔTEs) should be tested for a wider range of tissue quantification. Lastly, the design of the crusher gradient pair and the slice selection gradient should be improved and more designs of composite pulses should be tested to fully mitigate the problems arising from the mismatch of the slice profile.

Further research steps include testing the sequence on the brain and heart in an increased number of volunteers for a more sustained comparison of the results obtained with the values retrieved from literature. Additionally, breath hold experiments should be conducted to further validate the use of the GESE sequence for BOLD CMR techniques.

Bibliography

[1] Dwight G. Nishimura, *Principles of Magnetic Resonance Imaging*. Stanford University, 2010.

[2] A. G. Webb, *Introduction to Biomedical Imaging*. Wiley-IEEE Press, 2002.

[3] G. B. Chavhan, P. S. Babyn, B. Thomas, M. M. Shroff, and E. Mark Haacke, "Principles, techniques, and applications of T2*-based MR imaging and its special applications," *Radiographics*, vol. 29, no. 5, pp. 1433–1449, 2009.

[4] X. J. Z. MATT A. BERNSTEIN, KEVIN F. KING, *Handbook of MRI Pulse Sequences*, 2004.

[5] A. D. Elster, "Questions and Answers in MRI," 2015, accessed on December, 2021. [Online]. Available: https://mriquestions.com/complete-list-of-questions.html

[6] S. Abdulla, "Spatial Encoding," 2021, accessed on May 21, 2022. [Online]. Available: https://www.radiologycafe.com/frcr-physics-notes/mr-imaging/spatial-encoding/

[7] J. P. Ridgway, "Cardiovascular magnetic resonance physics for clinicians: Part i," *Journal of Cardiovascular Magnetic Resonance*, vol. 12, no. 1, p. 71, 2010. [Online]. Available: http://www.jcmr-online.com/content/12/1/71

[8] R. D. Dortch, "Quantitative T2 and T2* Mapping," in *Quantitative Magnetic Resonance Imaging*, 1st ed. Elsevier Inc., 2020, vol. 1, pp. 47–64. [Online]. Available: http://dx.doi.org/10.1016/B978-0-12-817057-1.00005-6

[9] M. K. Manhard, B. Bilgic, C. Liao, S. H. Han, T. Witzel, Y. F. Yen, and K. Setsompop, "Accelerated whole-brain perfusion imaging using a simultaneous multislice spin-echo and gradient-echo sequence with joint virtual coil reconstruction," *Magnetic Resonance in Medicine*, vol. 82, no. 3, pp. 973–983, 2019.

[10] K. E. Keenan, K. F. Stupic, M. A. Boss, and S. E. Russek, "Comparison of T1 measurement using ISMRM/NIST system phantom." 2016, accessed on November 10, 2021. [Online]. Available: https://www.nist.gov/publications/comparison-t1-measurement-using-ismrmnist-system-phantom

[11] “Magnetom Verio 3T,” accessed on November 10, 2021. [Online]. Available: https://www.mrc.wayne.edu/3t

[12] “Parasternal short axis view in the papillary plane,” https://theory.labster.com/parasternal_short_axis_papillary_view/, accessed: 2022-07-02.

[13] “Heart normal short axis echo,” https://pt.m.wikipedia.org/wiki/Ficheiro:Heart_normal_short_axis_echo.svg, accessed: 2022-07-02.

[14] “Short axis view,” http://radiology.con.mk/cardiacmr/Anatomy/Short.html, accessed: 2022-07-02.

[15] M. V. D. Boomen, M. K. Manhard, G. J. H. Snel, and S. Han, “Blood Oxygen Level – Dependent MRI of the Myocardium,” *Radiology*, vol. 294, no. 16, pp. 538–545, 2020.

[16] J. T. Skinner, R. K. Robison, C. P. Elder, A. T. Newton, B. M. Damon, and C. C. Quarles, “Evaluation of a multiple spin- and gradient-echo (SAGE) EPI acquisition with SENSE acceleration: Applications for perfusion imaging in and outside the brain,” *Magnetic Resonance Imaging*, vol. 32, no. 10, pp. 1171–1180, 2014. [Online]. Available: http://dx.doi.org/10.1016/j.mri.2014.08.032

[17] F. Bloch, “Nuclear induction,” *Phys. Rev.*, vol. 70, pp. 460–474, Oct 1946. [Online]. Available: https://link.aps.org/doi/10.1103/PhysRev.70.460

[18] D. Weishaupt, V. Kochli, B. Marincek, and E. E. Kim, *How Does MRI Work? An Introduction to the Physics and Function of Magnetic Resonance Imaging*, 2nd ed. Springer, 2006.

[19] M. Hammer, “MRI Physics: Tissue Contrast in MRI,” accessed on October 5, 2021. [Online]. Available: http://xrayphysics.com/contrast.html

[20] P. Rock, “Radiopaedia,” 2005-2022, accessed on December, 2021. [Online]. Available: https://radiopaedia.org/

[21] J. Z. Bojorquez, S. Bricq, C. Acquitter, F. Brunotte, P. M. Walker, and A. Lalande, “What are normal relaxation times of tissues at 3 T?” *Magnetic Resonance Imaging*, vol. 35, pp. 69–80, 2017. [Online]. Available: http://dx.doi.org/10.1016/j.mri.2016.08.021

[22] R. W. Brown, Y.-C. N. Cheng, E. M. Haacke, R. M. Thompson, and R. Venkatesan, *Magnetic Resonance Imaging: Physical Principles and Sequence Design*, 2nd ed. Hoboken: Wiley Blackwell, 2014.

[23] C. Roy, A. Slimani, C. De Meester, M. Amzulescu, A. Pasquet, D. Vancraeynest, J. L. Vanoverschelde, A. C. Pouleur, and B. L. Gerber, “Age and sex corrected normal reference values of T1, T2 T2$*$and ECV in healthy subjects at 3T CMR,” *Journal of Cardiovascular Magnetic Resonance*, vol. 19, no. 1, p. 72, 2017.

[24] R. Pohmann, O. Speck, and K. Scheffler, “Signal-to-noise ratio and mr tissue parameters in human brain imaging at 3, 7, and 9.4 tesla using current receive coil arrays,” *Magnetic Resonance in Medicine*, vol. 75, pp. 801–809, 2 2016.

[25] H. Schmiedeskamp, M. Straka, and R. Bammer, “Compensation of slice profile mismatch in combined spin- and gradient-echo echo-planar imaging pulse sequences,” *Magnetic Resonance in Medicine*, vol. 67, no. 2, pp. 378–388, 2012.

[26] M. Y. Tang, T. W. Chen, X. M. Zhang, and X. H. Huang, “GRE T2*-weighted MRI: Principles and clinical applications,” *BioMed Research International*, vol. 2014, p. 312142, 2014.

[27] H. Abdel-Aty, O. Simonetti, and M. G. Friedrich, “T2-weighted cardiovascular magnetic resonance imaging,” *Journal of Magnetic Resonance Imaging*, vol. 26, no. 3, pp. 452–459, 2007.

[28] H. Schmiedeskamp, M. Straka, R. D. Newbould, G. Zaharchuk, B. Jalal, J.-m. Olivot, M. E. Moseley, and G. W. Albers, “Combined Spin-And Gradient-Echo Perfusion-Weighted Imaging,” *Magnetic Resonance in Medicine*, vol. 68, no. 1, pp. 30–40, 2012.

[29] A. M. Stokes, J. T. Skinner, T. Yankeelov, and C. C. Quarles, “Assessment of a simplified spin and gradient echo (sSAGE) approach for human brain tumor perfusion imaging,” *Magnetic Resonance Imaging*, vol. 34, no. 9, pp. 1248–1255, 2016. [Online]. Available: http://dx.doi.org/10.1016/j.mri.2016.07.004

[30] S. Kaczmarz, F. Hyder, and C. Preibisch, “Oxygen extraction fraction mapping with multi-parametric quantitative BOLD MRI: Reduced transverse relaxation bias using 3D-GraSE imaging,” *NeuroImage*, vol. 220, no. February, p. 117095, 2020. [Online]. Available: https://doi.org/10.1016/j.neuroimage.2020.117095

[31] A. Prinster, C. Pierpaoli, R. Turner, and P. Jezzard, “Simultaneous measurement of ΔR2 and ΔR2* in cat brain during hypoxia and hypercapnia,” *NeuroImage*, vol. 6, no. 3, pp. 191–200, 1997.

[32] Y. Wang, R. Zhang, B. Zhang, C. Wang, H. Wang, X. Zhang, K. Zhao, M. Yang, X. Wang, and J. Zhang, “Simultaneous R2, R2’ and R2* measurement of skeletal muscle in a rabbit model of unilateral artery embolization,” *Magnetic Resonance Imaging*, vol. 61, no. May, pp. 149–157, 2019. [Online]. Available: https://doi.org/10.1016/j.mri.2019.05.030

[33] “What Are Imaging Phantoms? — NIST,” accessed on November 12, 2021. [Online]. Available: https://www.nist.gov/topics/physics/what-are-imaging-phantoms

[34] S. Fujita, A. Hagiwara, M. Hori, M. Warntjes, K. Kamagata, I. Fukunaga, C. Andica, T. Maekawa, R. Irie, M. Y. Takemura, K. K. Kumamaru, A. Wada, M. Suzuki, Y. Ozaki, O. Abe, and S. Aoki,

"Three-dimensional high-resolution simultaneous quantitative mapping of the whole brain with 3D-QALAS: An accuracy and repeatability study," *Magnetic Resonance Imaging*, vol. 63, no. June, pp. 235–243, 2019. [Online]. Available: https://doi.org/10.1016/j.mri.2019.08.031

[35] P. S. Myles and J. Cui, "Using the Bland-Altman method to measure agreement with repeated measures," *British Journal of Anaesthesia*, vol. 99, no. 3, pp. 309–311, 2007.

[36] "Bland-altman plot," https://www.medcalc.org/manual/bland-altman-plot.php, accessed: 2022-06-27.